

October 2002

ANL/TD/02-02
ANL-AAA-053

MEGAPIE Analytical Support Task: Characterization of Lead-Bismuth Eutectic and Sodium-Cooled Tungsten Target Materials for Accelerator Driven Systems

By

Yousry Gohar

Technology Development Division
Argonne National Laboratory
9700 South Cass Avenue
Argonne, IL 60439

Work supported by the
Office of Nuclear Energy
U.S. Department of Energy
Under Contract W-31-109-Eng-38

Table of Contents

	<u>Page</u>
Abstract.....	1
I. Introduction.....	2
II. Lead-Bismuth Target with Proton Beam	3
II.1. Energy Deposition	3
II.2 Neutron Yield.....	4
II.3 Neutron Spatial Distribution.....	4
II.4 Neutron Spectrum.....	5
II.5 Beam Window Nuclear Responses	5
II.6 Buffer Thickness Effect on the Nuclear Responses of the Structural Material and the Neutron Utilization	5
II.7 Target Length Effect on the Neutron Utilization.....	7
III. Lead-Bismuth Target with Deuteron Beam	7
IV. Tungsten Material with Proton Beam	8
IV.1. Energy Deposition	9
IV.2. Neutron Yield.....	9
IV.3. Neutron Spatial Distribution.....	10
IV.4. Neutron Spectrum.....	10
IV.5. Buffer Thickness Effect on the Nuclear Responses of the Structural Material and the Neutron Utilization	10
V. Sodium-Cooled Tungsten Target with Proton Beam.....	11
VI. Conclusions.....	12
References.....	14

List of Figures

<u>Figure No.</u>	<u>Page</u>
Figure 1. Lead-Bismuth target design concept	15
Figure 2. Sodium-cooled tungsten target design concept	16
Figure 3. Spatial energy deposition in the lead-bismuth eutectic for different proton energies with a uniform beam distribution normalized to the proton beam current density	17
Figure 4. Energy deposition in the lead-bismuth eutectic as a function of the proton energy normalized per incident proton on the right axis and per generated neutron on the left axis	17
Figure 5. Number of neutrons per proton and neutron percentage with energy above 20 MeV as a function of the proton energy from the lead-bismuth eutectic	18
Figure 6. Number of neutrons per proton leaving the lead-bismuth eutectic target boundaries as a function of the proton energy	18
Figure 7. Generated neutron distribution along the target buffer outer surface for different proton energies normalized per generated neutron from the lead-bismuth eutectic.....	19
Figure 8. Generated neutron distribution along the target buffer outer surface for different proton energies normalized per proton from the lead-bismuth eutectic	19
Figure 9. Generated high-energy ($E > 20$ MeV) neutron distribution along the target buffer outer surface for different proton energies normalized per proton from the lead-bismuth eutectic	20
Figure 10. Generated neutron spectra for different proton energies normalized per generated neutron from the lead-bismuth eutectic ...	20
Figure 11. Fission neutron spectrum compared to the lead-bismuth neutron spectrum generated by proton normalized per neutron.....	21
Figure 12. Number of generated neutrons per proton as a function of the buffer thickness from the lead-bismuth eutectic target for different proton energies	21

Figure 13. Neutron yield and neutron utilization as a function of the buffer thickness for the lead-bismuth eutectic target with 600-MeV proton beam.....	22
Figure 14. Neutron yield and neutron utilization as a function of the buffer thickness for the lead-bismuth eutectic target with 1000-MeV proton beam.....	22
Figure 15. Neutron yield and neutron utilization fraction as a function of the buffer thickness for the lead-bismuth eutectic target with 600- and 1000-MeV proton beams.....	23
Figure 16. Atomic displacement in the structural material outside the target as a function of the distance along the outer buffer boundary measured in the beam direction for the lead-bismuth eutectic target with 600-Mev proton beam and different buffer thicknesses ...	23
Figure 17. Helium gas production in the structural material outside the target as a function of the distance along the outer buffer boundary measured in the beam direction for the lead-bismuth eutectic target with 600-Mev proton beam and different buffer thicknesses.....	24
Figure 18. Hydrogen gas production in the structural material outside the target as a function of the distance along the outer buffer boundary measured in the beam direction for the lead-bismuth eutectic target with 600-Mev proton beam and different buffer thicknesses.....	24
Figure 19. Midplane nuclear responses in the structural material outside the target buffer as a function of the reciprocal of the outer buffer radius for the lead-bismuth eutectic target with 600-MeV proton beam.....	25
Figure 20. Helium to atomic displacement ratio in the structural material outside the target buffer as function of the buffer thickness of the lead-bismuth eutectic target with 600 MeV proton beam.....	25
Figure 21. Number of generated and utilized neutrons per 600-MeV proton as a function of the LBE target length.....	26
Figure 22. Number of generated and utilized neutrons per 1000-MeV proton as a function of the LBE target length.....	26
Figure 23. Spatial energy deposition in the lead-bismuth eutectic for different deuteron energies with a uniform beam distribution normalized to the deuteron beam current density	27

Figure 24. Energy deposition in the lead-bismuth eutectic as a function of the deuteron energy normalized per incident deuteron on the right axis and per generated neutron on the left axis	27
Figure 25. Number of neutrons per deuteron and neutron percentage with energy above 20 MeV as a function of the deuteron energy from the lead-bismuth eutectic	28
Figure 26. Number of neutrons per deuteron leaving the lead-bismuth eutectic target boundaries as a function of the deuteron energy.....	28
Figure 27. Generated neutron distribution along the target buffer outer surface for different deuteron energies normalized per deuteron from the lead-bismuth eutectic	29
Figure 28. Generated high-energy ($E > 20$ MeV) neutron distribution along the target buffer outer surface for different deuteron energies normalized per deuteron from the lead-bismuth eutectic.....	29
Figure 29. Generated neutron distribution along the target buffer outer surface for different proton and deuteron energies normalized per proton or deuteron from the lead-bismuth eutectic	30
Figure 30. Generated neutron spectra for different deuteron energies normalized per generated neutron from the lead-bismuth eutectic ...	30
Figure 31. Spatial energy deposition in the tungsten material for different proton energies with a uniform beam distribution normalized to the proton beam current density	31
Figure 32. Energy deposition in the tungsten material as a function of the proton energy normalized per incident proton on the right axis and per generated neutron on the left axis	31
Figure 33. Number of neutrons per proton and neutron percentage with energy above 20 MeV as a function of the proton energy from the tungsten material	32
Figure 34. Number of neutrons per proton leaving the tungsten material target boundaries as a function of the proton energy	32
Figure 35. Generated neutron distribution along the target buffer outer surface for different proton energies normalized per generated neutron from the tungsten material.....	33
Figure 36. Generated neutron distribution along the target buffer outer surface for different proton energies normalized per proton from the tungsten material	33

Figure 37. Generated high-energy ($E > 20$ MeV) neutron distribution along the target buffer outer surface for different proton energies normalized per proton from the tungsten material	34
Figure 38. Generated neutron spectra for different proton energies normalized per generated neutron from the tungsten material	34
Figure 39. Fission neutron spectrum compared to the neutron spectrum from the lead-bismuth eutectic and the tungsten material generated by proton normalized per neutron	35
Figure 40. Neutron spectra from the lead-bismuth eutectic and the tungsten material generated by proton normalized per neutron	35
Figure 41. Number of generated neutrons per proton as a function of the buffer thickness from the tungsten material for different proton energies.....	36
Figure 42. Neutron yield and neutron utilization as a function of the buffer thickness for the tungsten material with 600-MeV proton beam.....	36
Figure 43. Neutron yield and neutron utilization as a function of the buffer thickness for the tungsten material with 1000-MeV proton beam.....	37
Figure 44. Neutron yield and neutron utilization fraction as a function of the buffer thickness for the tungsten material with 600- and 1000-MeV proton beams.....	37
Figure 45. Number of generated neutrons per proton as a function of the buffer thickness for the sodium-cooled tungsten target with the 600-MeV proton beam	38
Figure 46. Atomic displacement in the structural material outside the target as a function of the distance along the outer buffer boundary measured in the beam direction for the for the sodium-cooled tungsten target with 600-Mev proton beam and different buffer thicknesses.....	38
Figure 47. Helium gas production in the structural material outside the target as a function of the distance along the outer buffer boundary measured in the beam direction for the for the sodium-cooled tungsten target with 600-Mev proton beam and different buffer thicknesses.....	39
Figure 48. Hydrogen gas production in the structural material outside the target as a function of the distance along the outer buffer boundary measured in the beam direction for the for the sodium-	

cooled tungsten target with 600-Mev proton beam and different
buffer thicknesses..... 39

Figure 49. Midplane nuclear responses in the structural material outside the
target thickness as a function of the reciprocal of the outer buffer
radius for the sodium-cooled tungsten target with 600-MeV
proton beam..... 40

Figure 50. Helium to atomic displacement ratio in the structural material
outside the target thickness as function of the buffer thickness of
the sodium-cooled tungsten target with 600 MeV proton beam 40

List of Tables

<u>Table No.</u>	<u>Page</u>
Table I. Target window nuclear responses from 600 MeV proton beam with 40 $\mu\text{A}/\text{cm}^2$ current density of the lead-bismuth target concept	41

MEGAPIE Analytical Support Task: Characterization of Lead-Bismuth Eutectic and Sodium-Cooled Tungsten Target Materials for Accelerator Driven Systems

Abstract

Lead-Bismuth Eutectic and Tungsten are under consideration as target materials with high-energy protons for generating neutrons to drive actinide and fission product transmuters. A detailed characterization has been performed to study the performance of these target materials as a function of the main variables and the design selections. The characterization includes the neutron yield, the spatial energy deposition, the neutron spectrum, the beam window performance, and the target buffer impact on the target performance. The characterization has also considered high-energy deuteron particles to study the impact on the target neutronic performance. The obtained results quantify the performance of the Lead-Bismuth Eutectic and Tungsten target materials as a function of the target variables and design selections.

MEGAPIE Analytical Support Task: Characterization of Lead-Bismuth Eutectic and Sodium-Cooled Tungsten Target Materials for Accelerator Driven Systems

I. Introduction

Lead-Bismuth Eutectic (LBE) technology is being developed worldwide for spallation neutron targets, which will drive subcritical transmuters [1 to 4]. This report is characterizing the performance of the LBE and tungsten target materials including the impact of the main variables and the design selections. The charged particle energy, the target buffer thickness, and the charged particle type are considered in the characterization. The performance analysis includes the neutron yield, the neutron utilization fraction, the neutron spatial distribution, the neutron spectrum, the energy deposition per generated neutron, the beam window nuclear responses, and the nuclear responses in the structural material outside the target buffer. The analysis was performed for proton and deuteron charged particles to define the impact on the LBE material performance. In the analysis process, heat transfer, hydraulics, beam window stresses, and target engineering issues have been considered to insure that the obtained performance is achievable from the target designs.

This work was performed using the spallation target design of the subcritical multiplier (SCM) of the accelerator driven test facility (ADTF) [4 to 6]. The ADTF is a nuclear research facility that will provide multiple testing and production capabilities. The ADTF target design is based on a coaxial geometrical configuration to satisfy the SCM configuration for minimizing the space requirements and to maximize the SCM utilization of the target neutrons. The target is installed vertically along the SCM axis. LBE is the target material and the target coolant. Ferritic steel (HT-9, Fe-12Cr-1Mo alloy) is the structural material for the target. The target coolant channels and the proton beam are entered vertically from the top above the SCM. The geometrical configuration shown in Figure 1 has been carefully designed to ensure flow stability and adequate cooling for the beam window and the structural material. The proton beam has a uniform spatial distribution over a circular cross section with 8-cm radius. The beam tube has 10-cm radius to accommodate the halo current. A hemi-spherical geometry is used for the beam window, which is connected to the beam tube. The beam tube is enclosed inside two coaxial tubes to provide inlet and outlet channels (manifolds) for the LBE coolant. In addition, the materials (LBE and target structure) between the beam trajectory and the boundary of the SCM (buffer) reduce the nuclear responses in the SCM structural material. The utilization of the LBE as a target, buffer, and coolant material does simplify the design. The target and beam configurations of the ADTF were adopted for the work presented in this paper.

The tungsten target replaces the LBE target of the ADTF. It uses the sodium coolant of the SCM to remove the deposited heat, which minimize the number of the ADTF coolant systems and avoid material computability issues with the SCM materials. The beam window has a hemi-spherical geometry and it is also cooled with sodium.

This target does not require the buffer to accommodate the target coolant channels, which leads to a minimum buffer thickness of 2-cm to accommodate the beam halo. In the analyses, the target region is homogenized with 65% tungsten and 35% sodium by volume to represent the design concept shown in Figure 2.

The MCNPX code [7] was used to perform the physics analysis. Each the MCNPX calculation used adequate source sampling in the range of 250000 to 1000000 source particles to achieve statistical error less than 1% within one standard deviation. The characterization results are presented as well as the main conclusions from the analysis. This report defines the design parameter values to operate the LBE and tungsten materials in spallation targets with a satisfactory performance. Also, recommendations are given to maximize the neutron utilization and to protect the structural material outside the target buffer from the high-energy neutrons.

II. Lead-Bismuth Target with Proton Beam

The Lead-bismuth target with proton beam was analyzed first and it is used as a reference to compare the performance of other target concepts or the impact of different design variables. Neutron yield, neutron utilization fraction, neutron spatial distribution, neutron spectrum, beam window nuclear responses, target buffer requirements, and nuclear responses in the structural material outside the target buffer are considered. The ADTF target design concept was used in the analyses.

II.1 Energy Deposition

The first step in the analysis was to define the required target length and the energy deposition profile in the LBE material for different proton energies. The proton energy considered is in the range of 200 to 1000 MeV. The results are shown in Figure 3, which are normalized to the incident proton current density. The peak energy deposition does not occur at the LBE surface but it is inside the LBE material along the beam axis. Such behavior is desirable because the beam window is not exposed to the peak heating value. Also, it does simplify the LBE heat removal. Increasing the charged particle energy reduces the peak power density and spreads the energy deposition in the lead-bismuth. As the proton energy increases above 600 MeV, the peak value shifts from the end of proton beam range to the beam entry area, at about 1 cm from the surface.

The total energy deposition increases linearly as the proton energy increases. However, the energy loss percentage to the endothermic reactions increases as the proton energy increases. The energy deposition per generated neutron shows a very fast decrease with the proton energy up to about 500 MeV, and then it slows down as shown in Figure 4. Such behavior encourages the use of high-energy protons to reduce the target cooling requirements for specific neutron source strength.

II.2 Neutron Yield

The total number of generated neutrons leaving the target per proton increases as the proton energy increases, as shown in Figure 5. This number includes the spallation neutrons and the secondary neutrons from the interactions of the high energy spallation neutrons with the LBE target material. Above 500 MeV proton energy, the number of generated neutrons per proton increases linearly with the proton energy. However, the neutron fraction with energy above 20 MeV reaches a saturation value of about 0.05 as the proton energy increases, as shown in Figure 5. The neutron utilization fraction is defined as the neutron fraction of the total generated neutrons that does not leave the target region in the beam direction since these neutrons have the opportunity to perform material transmutation. The neutrons leaving the target in the beam direction will interact with the shield, the reflector, or the transmuter structural material at the bottom of the target or travel in the beam tube above the target. The neutron utilization fraction changes from 0.53 at 200 MeV to 0.81 at 1000 MeV proton energy. As the proton energy increases, the neutrons are generated further away from the LBE surface, which increases the radial neutron leakage and subsequently the neutron utilization factor. The generated neutrons leaving the target region in the different directions (Top, Radial, and Bottom) are shown in Figure 6. In this analysis, an adequate target length is included to slow down, multiply, and reflect the neutrons at the end of the proton range (referred to as the bottom section). This enhances the neutron production per proton and the neutron utilization fraction. Also, a fixed buffer thickness of 7 cm of the LBE material is used in the analyses to protect the structural material of the SCM outside the target buffer and to function as input/output coolant channels for the LBE target material as shown in Figure 1. The effect of the buffer thickness on the neutron utilization fraction is discussed later. Again, these results show that increasing the proton energy is beneficial for enhancing the neutron yield as well as the neutron utilization factor.

II.3 Neutron Spatial Distribution

In the transmuter design, axial power peaking is a design issue, which has a significant impact on the transmuter performance. The spatial distribution of the generated neutrons has a direct impact on the power peaking in the driven systems. It is desirable to distribute uniformly the generated neutrons in the transmuter axial direction (beam direction) to reduce the power peaking. The spatial distribution of the generated neutron was calculated at the outer surface of the 7-cm buffer for different proton energies as shown in Figure 7 normalized per generated neutron. The results show that the uniformity of the generated neutron distribution in the beam direction improves as the proton energy increases. The neutron peak is reduced by a factor of two as the proton energy increases from 200 to 1000 MeV. Also, the neutron peak is shifted further by about 8 cm along the beam direction and the neutron spatial distribution spreads further along the beam axis. Figure 8 shows the generated neutron distribution normalized per proton, which confirms the spread and the shift of the neutron distribution with the increase in the proton energy in the beam direction. The high energy neutron distribution with neutron energy above 20 MeV in Figure 9 shows

similar distribution as the total generated neutrons. All the results show that the use of high proton energy helps reducing the axial power peaking in the driven transmuters.

II.4 Neutron Spectrum

The generated neutron spectra $n(E)$ at the outer buffer surface for different proton energies are shown in Figure 10. $n(E)$ is defined as the neutron fraction with energy E (MeV) per unit energy (MeV) interval normalized per generated neutron. The small wiggles in the neutron spectra between 0.045 and 0.075 MeV are due to the LBE resonance cross sections in this energy range. The neutron spectra are very similar up to 80 MeV. Above 80 MeV, the neutron spectra are reduced by a factor in the range of 10^4 to 10^8 relative to the peak value at 0.55 MeV. The average neutron energy is about 1 MeV compared to 2 MeV for the fission spectrum. The plotted neutron spectra represent the neutrons leaving the target buffer, which account for the interactions between the high-energy spallation neutrons and the LBE target material. These spectra include secondary neutrons from the (n,xn) interactions, and neutron slowing down through inelastic and elastic interactions. Figure 11 shows both the generated neutron spectra from Figure 10 and the fission spectrum. The generated neutron spectrum is softer than the fission spectrum; however it has a very high-energy tail as shown in Figure 10. This high-energy tail affects the nuclear responses in the structural material. It enhances the helium production rate, which affects the mechanical properties of the structural materials; further details are given in the buffer size section.

II.5 Beam Window Nuclear Responses

As an example, the nuclear responses in the beam window of the LBE target are given in Table 1 for the 600 MeV protons and the beam current is normalized to 40 $\mu\text{A}/\text{cm}^2$. The energy deposition density in the HT-9 beam window is 766.5 W/cm^3 and the peak value in the LBE material is 796 W/cm^3 at 1.75 cm from the LBE surface. The gas production and the atomic displacement cross sections used in the analyses account for the nuclear responses generated by the protons and the neutrons [8]. In the beam window, the neutrons produce 69% of the atomic displacement and the protons generate more than 96% of the gas production rate. The high gas production rate affects the mechanical properties of the window material, which requires experimental data for realistic lifetime prediction of the structural material. Structural analysis [4] utilizing experimental data with lower helium per atomic displacement shows that the beam window may be able to operate for full power year with 40 $\mu\text{A}/\text{cm}^2$ current density.

II.6 Buffer Thickness Effect on the Nuclear Responses of the Structural Material and the Neutron Utilization

The analysis was performed as a function of the buffer thickness. The cross section areas required for the inlet and the outlet LBE coolant channels define the minimum buffer thickness, which is 7 cm for 5 MW beam with 600 MeV protons [4 to 6].

The neutron yield (The total number of generated neutrons per proton leaving the target) has a low sensitivity to the buffer thickness as shown in Figure 12 to 15. The neutron yield reaches a saturation value at a buffer thickness of about 40 cm. The saturation value is about 1.14 times the value obtained with the 7-cm minimum buffer thickness. However, the number of neutrons utilized for material transmutation (the generated neutrons that reach the SCM) decreases significantly as the buffer thickness increases. The neutron utilization fraction drops from 0.71 with 7-cm buffer to 0.25 with 40-cm buffer as shown in Figures 13 and 14. The axial neutron leakage increases as the buffer thickness increases. This requires the target design to reduce the buffer thickness as much as possible.

The nuclear responses in the structural material outside the buffer zone are shown in Figures 16 through 18 as a function of the distance along the outer buffer boundary measured from the top of the SCM fuel in the beam direction for different buffer thicknesses. For a small buffer thickness, the results show that the peak values of the different nuclear responses occur near the SCM midplane. As the buffer thickness increases, the peak values of the gas production, helium and hydrogen, shift to the top section of the subcritical multiplier. On the other hand, the maximum atomic displacement stays at the SCM midplane. This means that the SCM fission neutrons are causing most of the nuclear responses for the small buffer thickness. For a constant total power of 100 MW, as the buffer thickness increases, the SCM volume increases to compensate for the increased neutron leakage. Therefore, the SCM average power density and the nuclear responses, which are dominated by the fission neutrons, are decreased. This explains the change in the gas production distribution as shown in Figures 17 and 18 where the contribution from the spallation neutrons are noticeable at the top section of the target and decrease along the target length for the large buffer sizes. However, the atomic displacement distribution maintains the peak value at the SCM midplane because the SCM fission neutrons are the main contributor.

The nuclear responses at the SCM midplane are shown as a function of the reciprocal of the outer buffer radius in Figure 19. The results show a good linear fit because the fission neutrons dominate the reaction rates at the SCM boundary. The other important parameter for the structural material performance is the helium to atomic displacement ratio. Figure 20 shows this ratio as a function of the buffer thickness, which is in the range of 0.1 to 0.3. This ratio is about 0.26 for HT-9 in a typical fast reactor spectrum. These results show that the 7-cm buffer thickness protects the structural material from the nuclear responses caused by the high energy neutrons ($E > 20$ MeV), utilizes most of the spallation neutrons for driving the subcritical multiplier, and has adequate cross section area for the inlet and the outlet coolant channels. Therefore, the lifetime of the structural material around the buffer will depend on the operating temperature, the nuclear responses, and the loading conditions similar to fast fission systems.

II.7 Target Length Effect on the Neutron Utilization

The required target length to stop the proton beam is obtained from the axial energy deposition profile. The energy deposition profile is shown in Figure 3 as a function of the distance along the beam axis for proton energy in the range of 200 to 1000 MeV. The required target length is ~32 and ~64 cm to stop the 600- and 1000-MeV protons, respectively. The peak energy deposition is 20.8 and 25 W/cm³/(μA/cm²) at 1.65 and 2.65 cm from the LBE surface, respectively. Engineering and neutron yield considerations require extending the target length. The thermal-hydraulics analyses require a small target length extension to insure the flow stability of the lead-bismuth eutectic in the target area and the appropriate temperature distribution in the target structure [4], which represents the minimum extension length. The neutron yield was analyzed as a function of the target length for 600- and 1000-MeV protons. Figures 21 and 22 give the total and the utilized neutrons in terms of neutrons per proton normalized to the results from the 80 cm target length. The results show that the neutron yield reaches saturation as the target length increases. For the 600 MeV proton beam, a target length of 38 cm (6 cm extension) generates ~98% of the total possible neutrons and utilizes ~90% of the utilized neutrons of the 80 cm target. However, the 1000 MeV proton beam does not require any extension from the physics point of view as can be seen from the results of Figure 22. The thermal-hydraulics defines the target extension length for the target with the 1000-MeV proton beam.

III. Lead-Bismuth Target with Deuteron Beam

Another characterization for the LBE material performance was performed with deuterons instead of protons. The deuteron energy was varied in the range of 200 to 1000 MeV similar to the proton characterization. The energy deposition profile in the LBE for different deuteron energies is shown in Figure 23 and the results are normalized to the deuteron current density. The deuteron energy deposition profiles are similar to the proton profiles. However the range of the deuterons with Energy E is about twice the range of the proton with energy E/2. Also, the peak energy deposition from the deuterons is about twice the corresponding value for the protons with same energy. This means that the neutrons are generated over shorter range, which has positive impact on the transmuters as will be discussed later and negative impact on the thermal hydraulics.

Similar to the proton case, the total energy deposition and the neutron production increase as the deuteron energy increases. The Deuteron generates slightly more energy and neutrons than the proton of the same energy. In the energy range of 400 to 1000 MeV, the deuteron generates about 7 to 9% more neutrons relative to the proton. The deuteron has a shorter range, which increases the probability for the forward high-energy spallation neutrons to multiply through (n,xn) interactions and to slow down through elastic and inelastic interactions with the LBE material. The resulting neutron spectrum is slightly softer because of these interactions. Similar to the proton beam, the total energy deposition increases linearly as the deuteron energy increases. Also, the energy loss percentage to the endothermic reactions increases as the deuteron energy

increases. The energy deposition per generated neutron shows a very fast decrease with the deuteron energy up to about 500 MeV, and then it slows down as shown in Figure 24. Such behavior encourages the use of high-energy deuterons to reduce the target cooling requirements for specific neutron source strength.

The total number of generated neutrons per proton increases as the deuteron energy increases as shown in Figure 25. This number includes the spallation neutrons and the secondary neutrons from the interactions of the high energy spallation neutrons with the LBE target material. Above 500 MeV deuteron energy, the number of generated neutrons per proton increases linearly with the deuteron energy. However, the neutron fraction with energy above 20 MeV reaches a saturation value of ~ 0.06 as the deuteron energy increases, as shown in Figure 25. The neutron utilization fraction changes from 0.57 at 200 MeV to 0.81 at 1000 MeV proton energy. As the proton energy increases, the neutrons are generated further away from the LBE surface, which increases the radial neutron leakage and subsequently the neutron utilization factor. The generated neutrons leaving the target in the different directions (Top, Radial, and Bottom) are shown in Figure 26. An adequate target length is included to slow down, multiply, and reflect the high-energy neutrons at the end of the deuteron range (referred to as the bottom section). This enhances the neutron production per deuteron and the neutron utilization fraction. Also, a fixed buffer thickness of 7 cm LBE material is used in the analyses to protect the structural material of the SCM outside the target buffer and to function as input/output coolant channels for the LBE target material as shown in Figure 1. These results show that the use of high-energy deuteron is beneficial for enhancing the neutron yield as well as the neutron utilization factor.

The spatial distribution of the generated neutron was calculated at the outer surface of the 7-cm buffer for different deuteron energies as shown in Figure 27 normalized per deuteron. The results show that the uniformity of the generated neutron distribution in the beam direction improves as the proton energy increases. The high energy neutron distribution with neutron energy above 20 MeV in Figure 28 shows similar distribution as the total generated neutrons. All the distributions of Figures 27 and 28 are similar to the distributions of the proton beam. Figure 29 compares the generated neutron distribution along the target buffer outer surface for different proton and deuteron energies, which shows the deuteron generating more neutrons than the proton with similar spatial distribution. However, there are other issues related to the use of deuterons including the accelerator cost, which require cost-benefit analyses to select between proton and deuteron. The obtained neutron spectra are shown in Figure 30 for deuteron with energy in the range of 200- to -1000MeV

IV. Tungsten Material with Proton Beam

The lead-bismuth eutectic target analyses with proton beam were performed for the sodium-cooled tungsten target. First the analyses used pure tungsten material without the sodium coolant to define the performance of the tungsten target material. Then the analyses were carried out for the sodium-cooled tungsten target to

characterize its performance. The obtained results are compared to the results of the LBE target.

IV.1. Energy Deposition

The energy deposition profiles in the tungsten material for proton energies in the range of 200 to 1000 MeV are shown in Figure 31, which are normalized to the incident proton current density. The peak energy deposition does not occur at the tungsten surface but it is inside the tungsten material along the beam axis similar to the LBE material. Increasing the charged particle energy reduces the peak power density and spreads the energy deposition in the tungsten material. As the proton energy increases above 600 MeV, the peak value shifts from the end of proton beam range to the beam entry area, at about 1 cm from the surface. Also, the peak energy deposition value in tungsten is more than double that of the LBE material and the proton range in the tungsten material is about half that of the LBE material for the same proton energy.

The total energy deposition increases linearly as the proton energy increases but it is lower than the corresponding value from the LBE material. The energy loss percentage to the endothermic reactions increases as the proton energy increases. The energy deposition per generated neutron shows a very fast decrease with the proton energy up to about 500 MeV, and then it slows down as shown in Figure 32. Such behavior encourages the use of high-energy protons to reduce the target cooling requirements for specific neutron source strength.

IV.2 Neutron Yield

The total number of generated neutrons per proton is shown as a function of the proton energy in Figure 33. This number includes the spallation neutrons and the secondary neutrons from the interactions of the high energy spallation neutrons with the tungsten target material. Above 500 MeV proton energy, the number of generated neutrons per proton increases linearly with the proton energy. However, the neutron fraction with energy above 20 MeV reaches a saturation value of about 0.05 as the proton energy increases similar to the LBE material, as shown in Figure 33. For the same proton energy, the LBE material generates more neutrons per proton as shown by comparing the results from Figures 4 and 33. The generated neutrons leaving the target region in the different directions (Top, Radial, and Bottom) are shown in Figure 34. In this analysis, an adequate target length is included to slow down, multiply, and reflect the high-energy neutrons at the end of the proton range (referred to as the bottom section). A fixed buffer thickness of 2 cm of the tungsten material is used in the analyses to accommodate the beam halo. The effect of the buffer thickness on the neutron utilization fraction is discussed later. Again, these results show that the use of the high-energy protons is beneficial for enhancing the neutron yield as well as the neutron utilization factor.

IV.3 Generated Neutron Spatial Distribution

The spatial distribution of the generated neutron was calculated at the outer surface of the 2-cm buffer for different proton energies as shown in Figure 35 normalized per generated neutron. The results show that the uniformity of the generated neutron distribution in the beam direction improves as the proton energy increases. The neutron peak is reduced by a factor of two as the proton energy increases from 200 to 1000 MeV. Also, the neutron peak is shifted further by about 4.5 cm along the beam direction and the neutron spatial distribution spreads further along the beam axis. Figure 36 shows the generated neutron distribution normalized per proton, which confirms the spread and the shift of the neutron distribution with the increase in the proton energy in the beam direction. The high energy neutron distribution with neutron energy above 20 MeV in Figure 37 shows similar distribution as the total generated neutrons. All the results show that the use of high proton energy helps reducing the axial power peaking in the driven transmuters. The generated neutron distributions of the tungsten and the LBE materials are similar except the range is about doubled in the case of LBE material for the same proton energy.

IV.4 Neutron Spectrum

The generated neutron spectra $n(E)$ at the outer buffer surface are shown in Figure 38 for different proton energies. The neutron spectra are very similar up to 80 MeV. Above 80 MeV, the neutron density is reduced by a factor in the range of 10^4 to 10^8 relative to the peak value at 0.1 MeV. The plotted neutron spectra represent the neutrons leaving the target buffer, which account for the interactions between the high-energy spallation neutrons and the tungsten target material. These spectra include secondary neutrons from the (n, xn) interactions, and neutron slowing down through inelastic and elastic interactions. Figure 39 compares the neutron spectra from the LBE and the tungsten materials, and the fission spectrum. The fission spectrum is harder than the spectra from both materials. However, the high-energy tails of the generated spectra affect the nuclear responses in the structural material. It enhances the helium production rate, which affects the mechanical properties of the structural materials; further details are given in the buffer size section. The tungsten neutron spectrum with 600-MeV protons is compared to the corresponding spectrum for the LBE material in Figure 40 to show that the tungsten material has softer neutron spectrum relative to the LBE material.

IV.5 Buffer Thickness Effect on the Nuclear Responses of the Structural Material and the Neutron Utilization

The neutron yield was analyzed for this tungsten material as a function of the buffer thickness for 600- and 1000-MeV proton energies. A 2-cm is the minimum buffer thickness required to accommodate the beam halo. Figure 41 shows the obtained results, which indicate different behavior from the LBE results. For the same proton energy, the neutron yield decreases as the buffer thickness increases because the

neutron absorption in the tungsten is greater than the neutron multiplication through (n, xn) interactions. The tungsten buffer is more efficient in reducing the neutron fraction with energy above 20 MeV relative to the LBE buffer as shown in Figure 41. Tungsten has higher inelastic cross section than LBE that slows down the high energy component of the neutron spectrum. The tungsten buffer has also a strong negative effect on the neutron utilization as shown in Figures 42 and 43 for the two proton energies under consideration. The neutron utilization factor of the 600 MeV proton beam is less than that of 1000 MeV for the same buffer thickness as shown in Figure 44. The neutrons generated from the 600-MeV proton interactions are born over much shorter section of the target relative to 1000-MeV case as can be seen from Figure 31, which results in more neutron interaction inside the target including parasitic absorption. The required tungsten target length is less than half of the LBE target for the same proton energy as can be seen by comparing the results of Figures 3 and 31.

V. Sodium-Cooled Tungsten Target with Proton Beam

In the tungsten target, the sodium coolant is used to remove the energy deposition. The tungsten material volume fraction in the target region is 65%, which extends the target length by a factor of 1.54 to stop the proton beam. The buffer analyses were performed to account for the sodium coolant and the neutron yield results are shown in Figure 45. The sodium coolant reduces the neutron yield and changes the effect of the buffer thickness on the neutron yield as shown in Figure 45. The neutron yield reaches a peak at about 6.5-cm thick buffer. The peak value has ~2.6% more neutrons compared to the neutron production with 2-cm buffer required for the beam halo. The sodium coolant increases the proton scattering and reduces the slowing down characteristics of the target, which causes the positive effect from increasing the buffer thickness with respect to the neutron yield. However, the neutron utilization factor is reduced as the buffer thickness increases, which calls also for the use of the smallest buffer thickness.

The nuclear responses in the structural material outside the buffer of the sodium-cooled tungsten target are shown in Figures 46 through 48 as a function of the distance along the outer buffer boundary measured from the top surface of the 100-MW SCM fuel for different buffer thicknesses with 5 MW beam power and 600-MeV protons. The total SCM power is maintained at 100 MW with 5 MW beam power using 600-MeV protons. The results show similar behavior to the results from the LBE target. For the same buffer thickness, the nuclear responses, atomic displacement and gas production of the sodium-cooled tungsten target, are lower than the corresponding values from the LBE target. The difference in the inelastic cross section of both target materials is responsible for the difference in the nuclear responses. Figure 49 shows the nuclear responses at the SCM midplane as a function of the reciprocal of the outer buffer radius, which have a good linear fit similar to the LBE target results. The helium to the atomic displacement ratio is about twice the corresponding value for the LBE target without buffer. As the buffer thickness increases, the difference between the two ratios is reduced. At 18-cm buffer thickness, this ratio is ~0.1 for both targets as shown in Figures 20 and 50.

VI. Conclusions

The characterization results of Lead-Bismuth Eutectic and sodium-cooled tungsten target materials for accelerator driven systems presented in this report reached the following main conclusions:

1. The neutron yield increases with the proton energy. However the high-energy neutron fraction ($E > 20$ MeV) is not sensitive to the proton energy and it is less than 6% of the total generated neutrons.
2. Increasing the proton energy reduces the peak power density and spreads the energy deposition in the target materials. Such effects reduce the maximum window temperature and facilitate the heat removal from the target.
3. The total energy deposition per generated neutron decreases fast as the charged particle energy increases up to ~ 600 MeV, then it decreases slowly.
4. The uniformity of the generated neutron distribution increases in the beam direction as the energy of the charged particles increases. The peak value is always shifted away from the beam entry surface. Increasing the uniformity of the generated neutron distribution is desirable for reducing the axial power peaking in the transmuters.
5. The high-energy neutrons ($E > 20$ MeV) and the total neutrons have similar spatial distribution with more shifting for the peak value of the high energy neutrons in the beam direction away from the beam entry surface.
6. The generated neutron spectra do not change with the energy of the charged particles except for the upper end of the spectra above 80 MeV. At this high neutron energy, the neutron densities are 4 to 8 orders of magnitude less than the peak value.
7. The average energy of the generated neutrons with 7-cm buffer for the LBE target or 2-cm buffer for the sodium-cooled tungsten target is less than 1 MeV compared to 2 MeV for fission neutron spectrum. However, the high-energy tail of the target neutron spectra affects the nuclear responses in the structural materials.
8. The use of 7-cm buffer for lead-bismuth eutectic target, which is required for the inlet and outlet coolant channels, or 2-cm buffer for the sodium-cooled tungsten target, which is required to accommodate the beam halo reduces the nuclear responses in the structural material around the target buffer to the observed values in the fast fission reactors.
9. The nuclear responses in the structural material outside the target buffer are dominated by the transmuter. Consequently, the nuclear responses at the SCM midplane show a good linear fit with the reciprocal of the outer buffer radius for a constant transmuter power.

10. The neutron balance analysis shows that the large buffer thickness reduces significantly the neutron utilization factor. For example, at 40-cm buffer thickness for the LBE target, the neutron utilization factor is 0.25, which means a beam power loss of 75%.
11. In the lead-bismuth eutectic target, the required axial target extension is a function of the proton energy. A 6-cm target extension is needed for the 600 MeV protons. As the proton energy increases to 1000 MeV, no extension is needed. At this proton energy, the thermal-hydraulics analyses define the required extension
12. In the lead-bismuth eutectic target, the range of the deuteron with energy E is about twice the range of the proton with energy $E/2$. Also, the peak energy deposition from the deuteron is about twice the corresponding value for the proton with same energy.
13. In lead-bismuth, deuterons produce slightly more neutrons than protons. For the same axial target length and beam particle energy, the difference is about 7 to 9 % for the deuterons in the energy range of 400 to 1000 MeV. Other issues including the beam generation cost require further analyses to judge the value of generating more neutrons per charged particle.

References

1. A. Dedoul, B. Gromov, E. Yefimov, E. Zemskov, K. Ivanov, M. Leonchuk, Yu. Orlov, D. Pankratov, Z. Sivack, V. Troyanov, N. Khaveyev, V. Chitaykin, V. Chekunov, N. Klimov, M. Koulikov, V. Stepanov, T. Kitano, M. Ono, "Conceptual Design of Molten Lead-Bismuth Target Complex of Integral Type for ADS," Accelerator Applications/Accelerator Driven Transmutation Technology and Applications 01 (AccApp-ADTTA'01), Reno, Nevada, November 2001.
2. Joachim U. Knebel, Jean-Christophe Klein, Dominique Gorse, Pietro Agostini, Friedrich Gröschel, Peter Kupschus, Thomas Kirchner, Jean-Bernard Vogt, "MEGAPIE-TEST: A European Project on Spallation Target Testing," Accelerator Applications/Accelerator Driven Transmutation Technology and Applications 01 (AccApp-ADTTA'01), Reno, Nevada, November 2001.
3. A. Dedoul, S. Grishakov, Ye. Yefimov, Ye. Zemskov, M. Leonchuk, D. Pankratov, D. Rachkova, Z. Sivak, V. Chitaykin, V. Chekunov, S. Sidorkin, F. Perekretenko, V. Stepanov, N. Klimov, M. Kulikov, "Concept of Lead-Bismuth Liquid Metal Target for Proton Accelerator of Moscow Meson Plant," Accelerator Applications/Accelerator Driven Transmutation Technology and Applications 01 (AccApp-ADTTA'01), Reno, Nevada, November 2001.
4. Yousry Gohar, Phillip J. Finck, Lubomir Krajtl, Joseph E. Herceg, W. David Pointer, James Saiveau, Tanju Sofu, Albert L. Hanson, Michael Todosow, Maria Koploy and Panto Mijatovic, "Lead- Bismuth Target Design for the Subcritical Multiplier (SCM) of the Accelerator Driven Test Facility (ADTF)," Argonne National Laboratory Report, ANL/TD/02-01, 2002.
5. Y. Gohar, J. Herceg, L. Krajtl, D. Pointer, J. Saiveau, T. Sofu, and P. Finck, "Lead-Bismuth-Eutectic Spallation Neutron Source for Nuclear Transmuter," Accelerator Applications/Accelerator Driven Transmutation Technology and Applications 01 (AccApp-ADTTA'01), Reno, Nevada, November 2001.
6. David Pointer, Tanju Sofu, and Yousry Gohar, "Optimization of a Liquid Lead-Bismuth Eutectic Spallation Target Using Computational Fluid Dynamics," Paper submitted for presentation and publication in the Proceedings of ASME FEDSM'02, 2002 ASME Fluids Engineering Division Summer Meeting, Montreal, Quebec, Canada, July 14-18, 2002.
7. MCNPX Team, "MCNPX Version 2.4.j," Los Alamos National Laboratory, LA-UR-02-2127 (25 March, 2002).
8. Eric Pitcher, "Elemental Neutron- and Proton-Induced Displacement and Gas Production Cross Sections for Incident Particle Energies Ranging from 16 to 3120 MeV," paper presented at Accelerator Applications/Accelerator Driven Transmutation Technology and Applications 01 Meeting (AccApp-ADTTA'01), Reno, Nevada, November 2001; and Eric Pitcher, Private Communication, 2001.

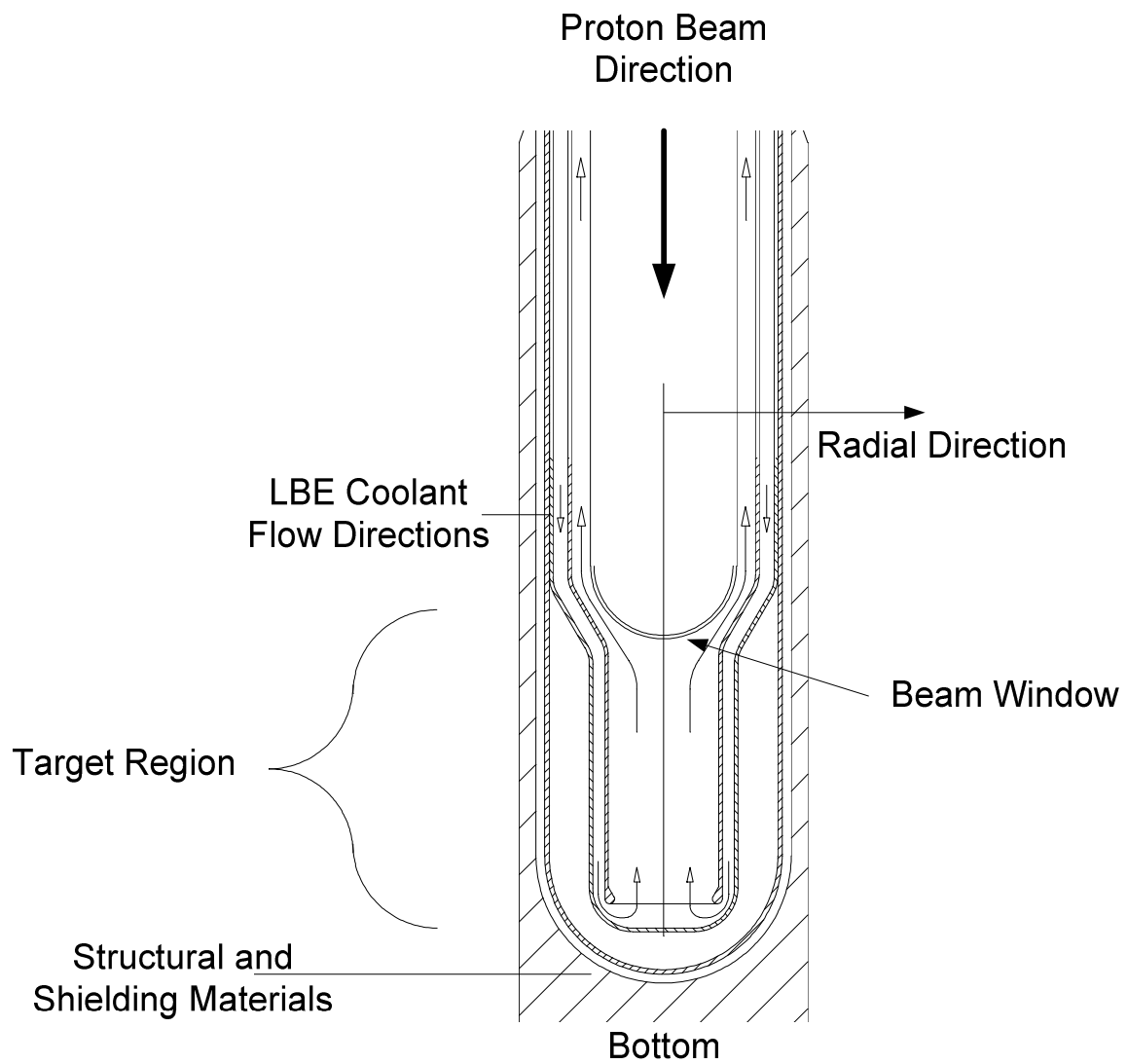


Figure 1. Lead-Bismuth target design concept

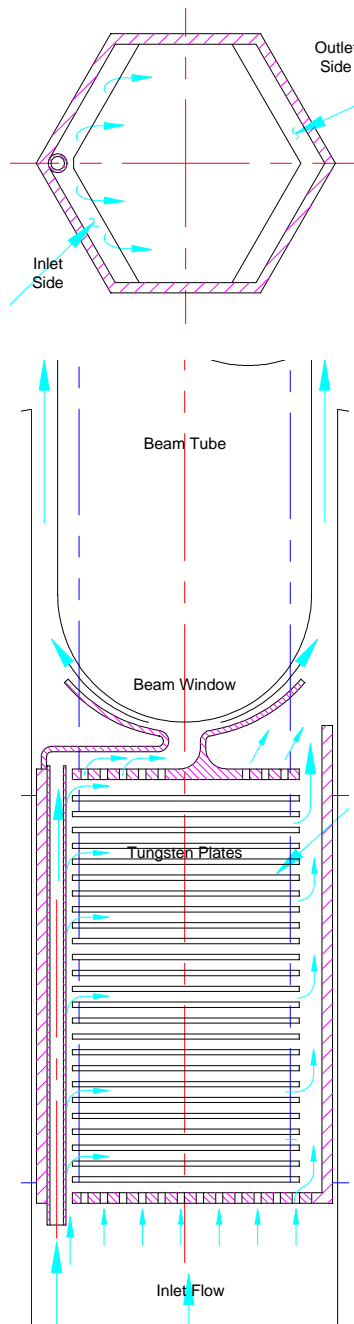


Figure 2. Sodium-cooled tungsten target design concept

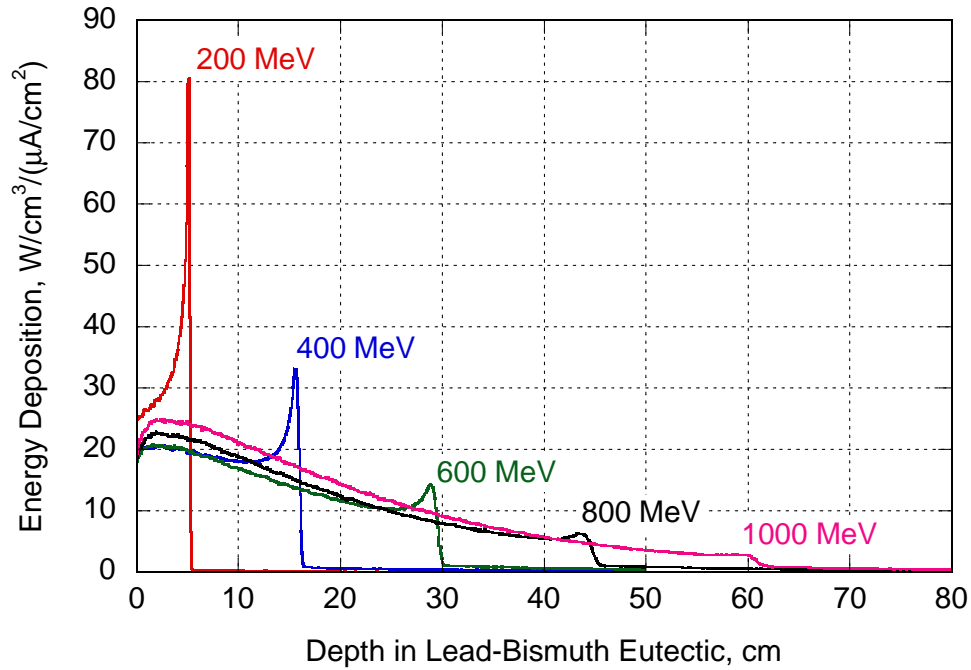


Figure 3. Spatial energy deposition in the lead-bismuth eutectic for different proton energies with a uniform beam distribution normalized to the proton beam current density

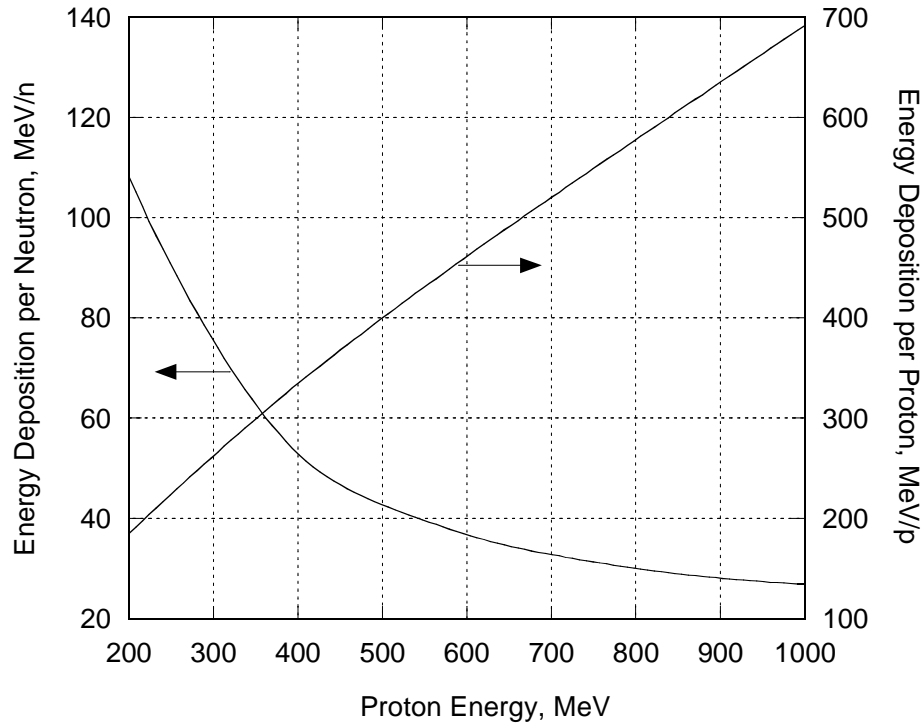


Figure 4. Energy deposition in the lead-bismuth eutectic as a function of the proton energy normalized per incident proton on the right axis and per generated neutron on the left axis

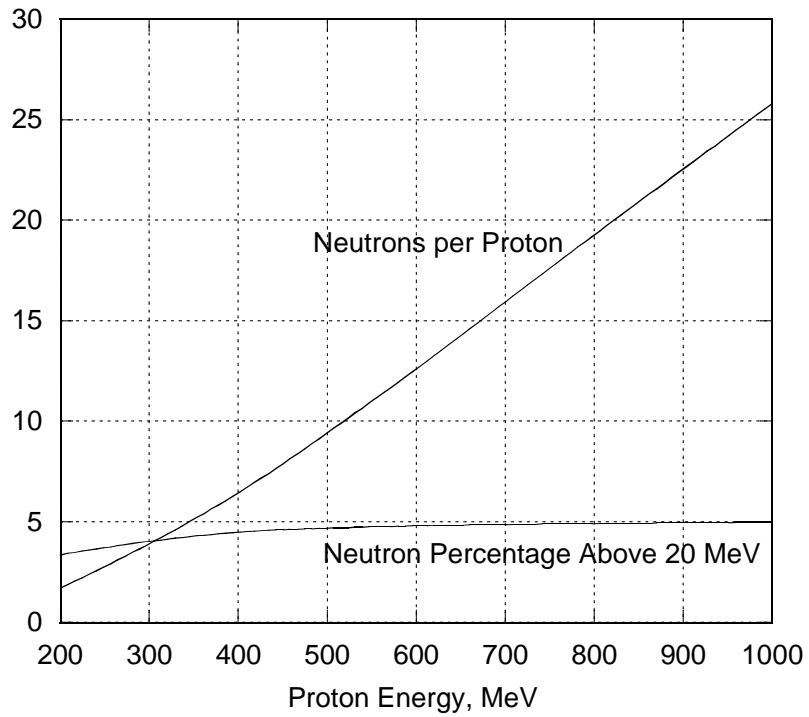


Figure 5. Number of neutrons per proton and neutron percentage with energy above 20 MeV as a function of the proton energy from the lead-bismuth eutectic

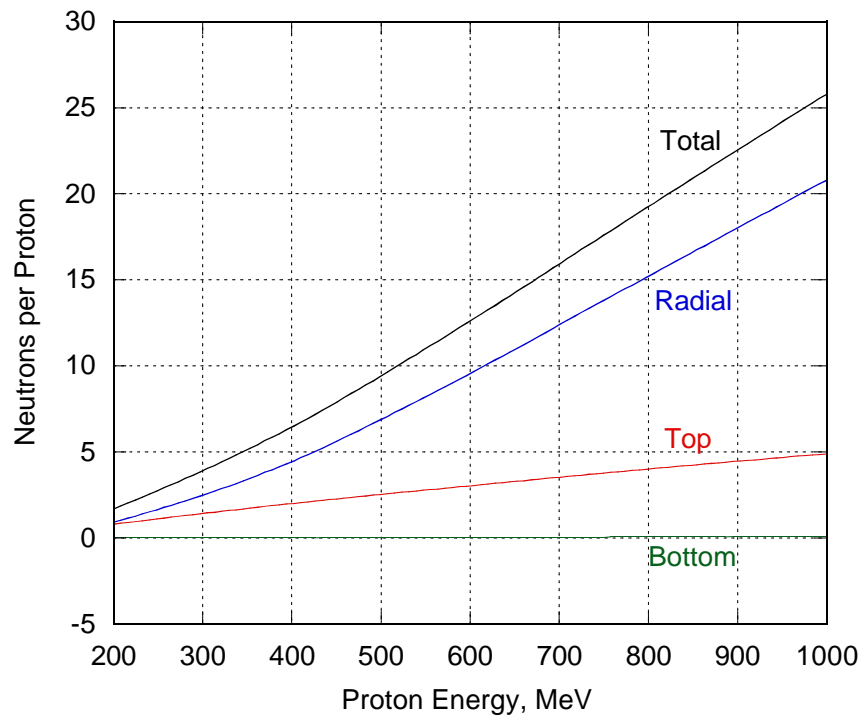


Figure 6. Number of neutrons per proton leaving the lead-bismuth eutectic target boundaries as a function of the proton energy

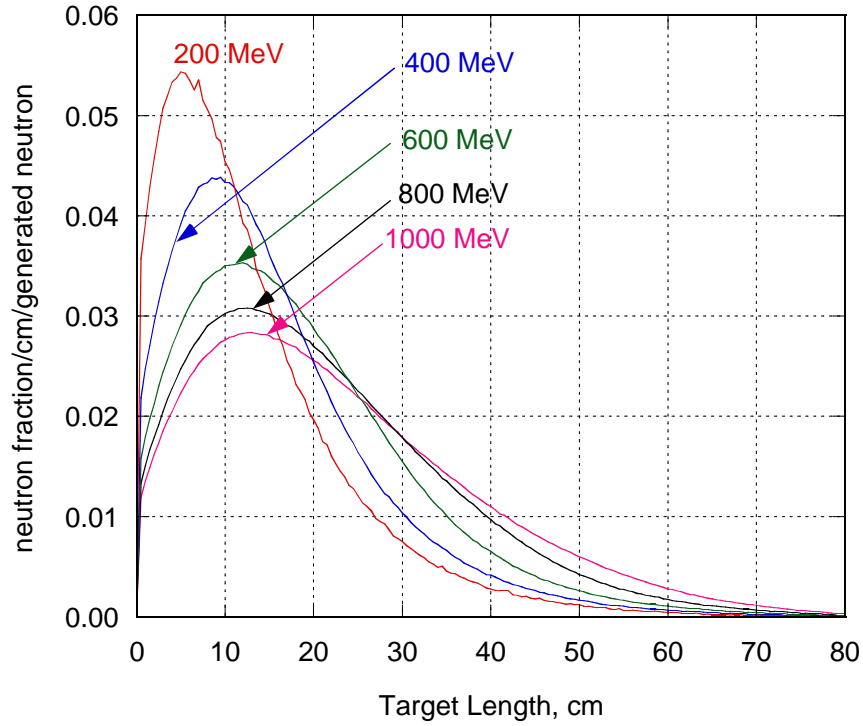


Figure 7. Generated neutron distribution along the target buffer outer surface for different proton energies normalized per generated neutron from the lead-bismuth eutectic

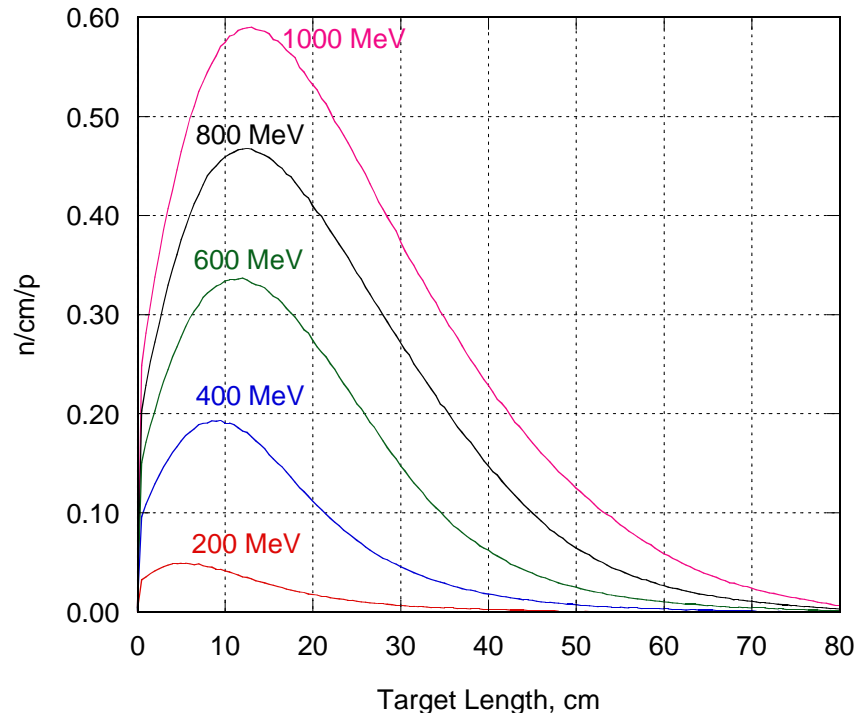


Figure 8. Generated neutron distribution along the target buffer outer surface for different proton energies normalized per proton from the lead-bismuth eutectic

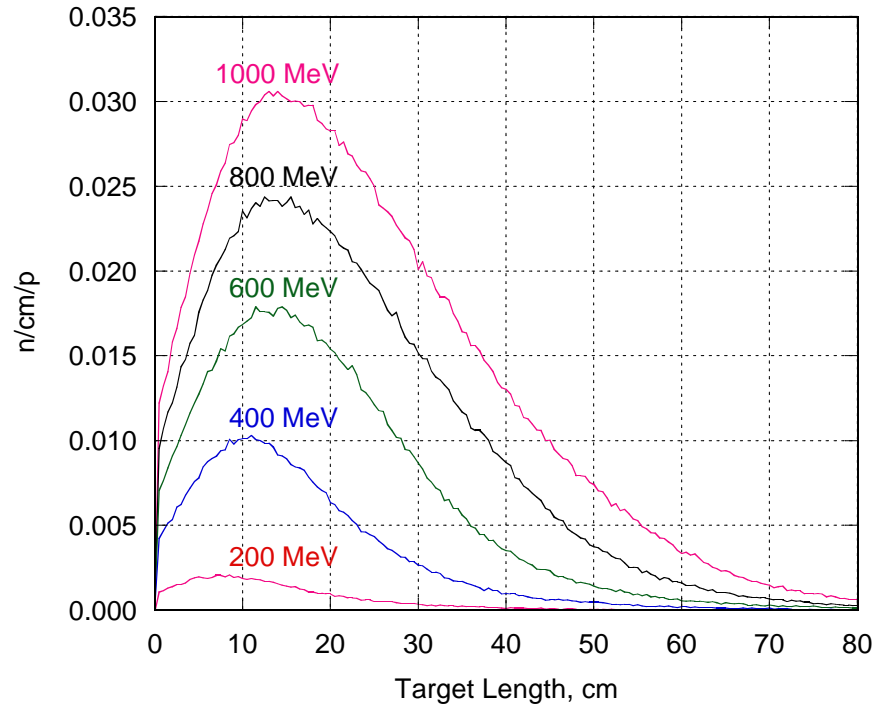


Figure 9. Generated high-energy ($E > 20$ MeV) neutron distribution along the target buffer outer surface for different proton energies normalized per proton from the lead-bismuth eutectic

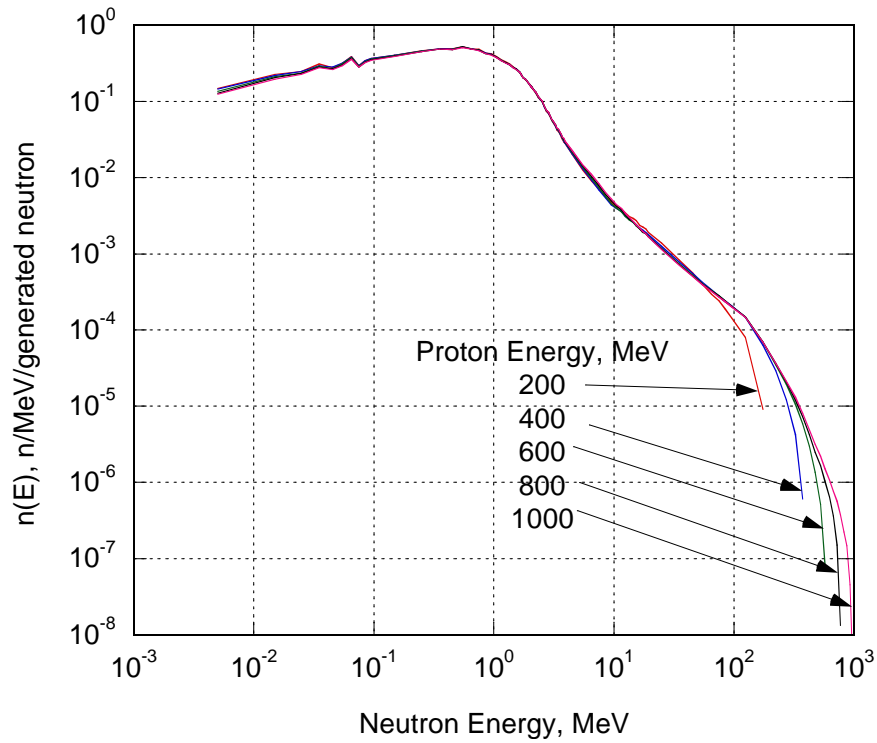


Figure 10. Generated neutron spectra for different proton energies normalized per generated neutron from the lead-bismuth eutectic

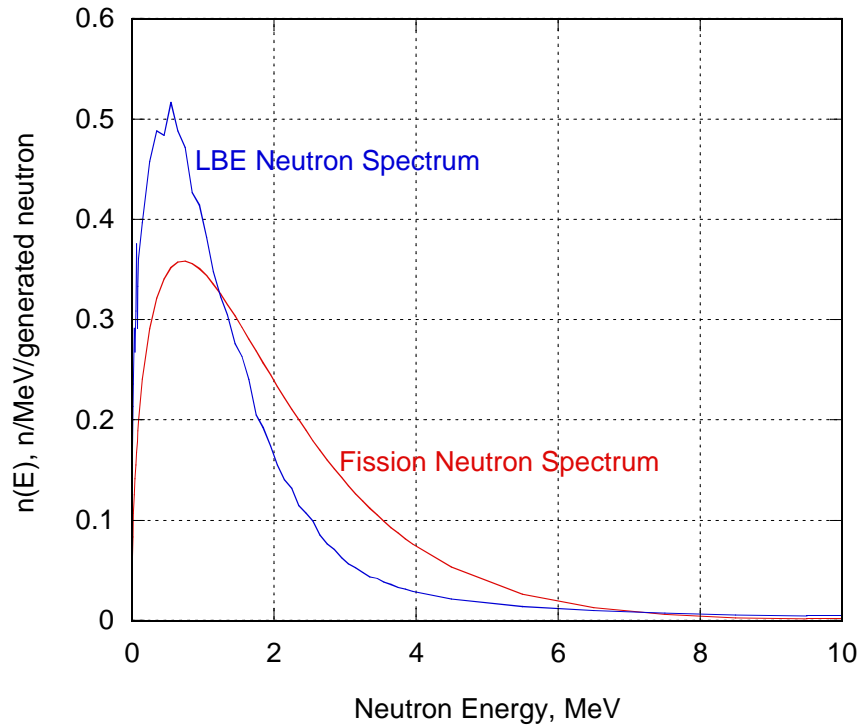


Figure 11. Fission neutron spectrum compared to the lead-bismuth neutron spectrum generated by proton normalized per neutron

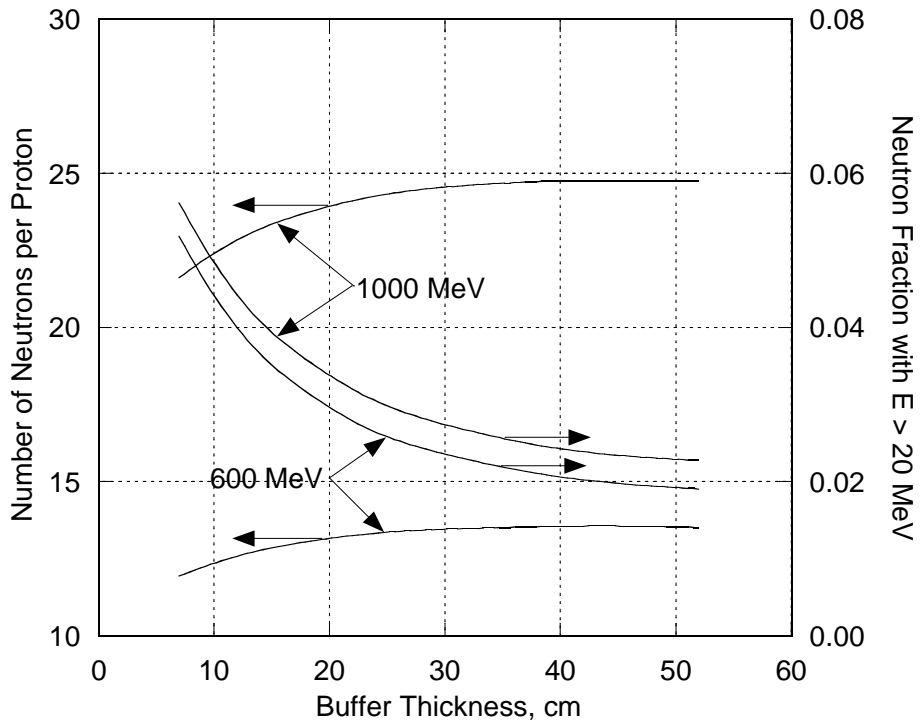


Figure 12. Number of generated neutrons per proton as a function of the buffer thickness from the lead-bismuth eutectic target for different proton energies

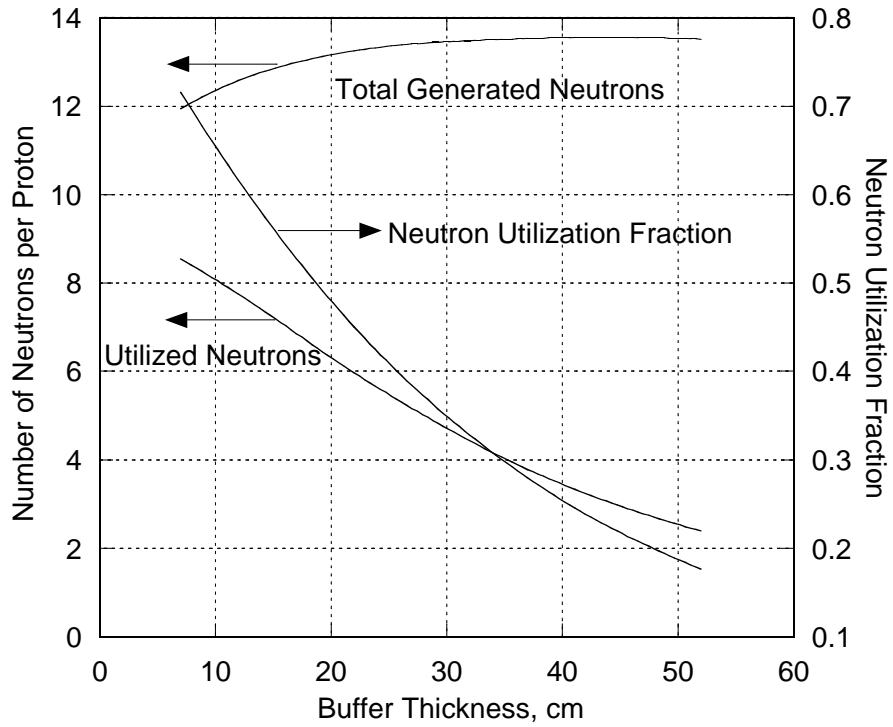


Figure 13. Neutron yield and neutron utilization as a function of the buffer size for the lead-bismuth eutectic target with 600-MeV proton beam

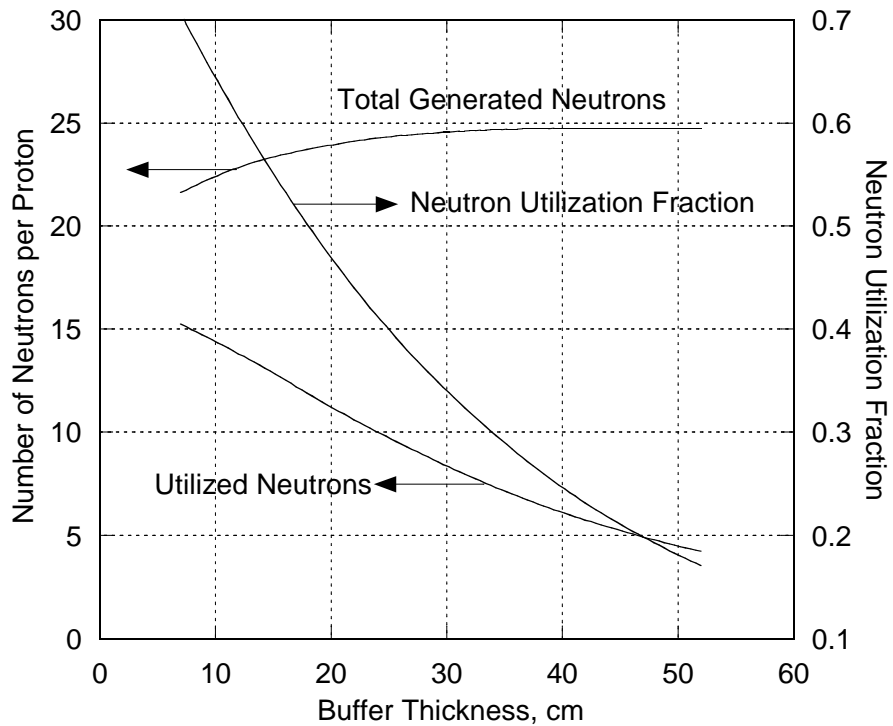


Figure 14. Neutron yield and neutron utilization as a function of the buffer size for the lead-bismuth eutectic target with 1000-MeV proton beam

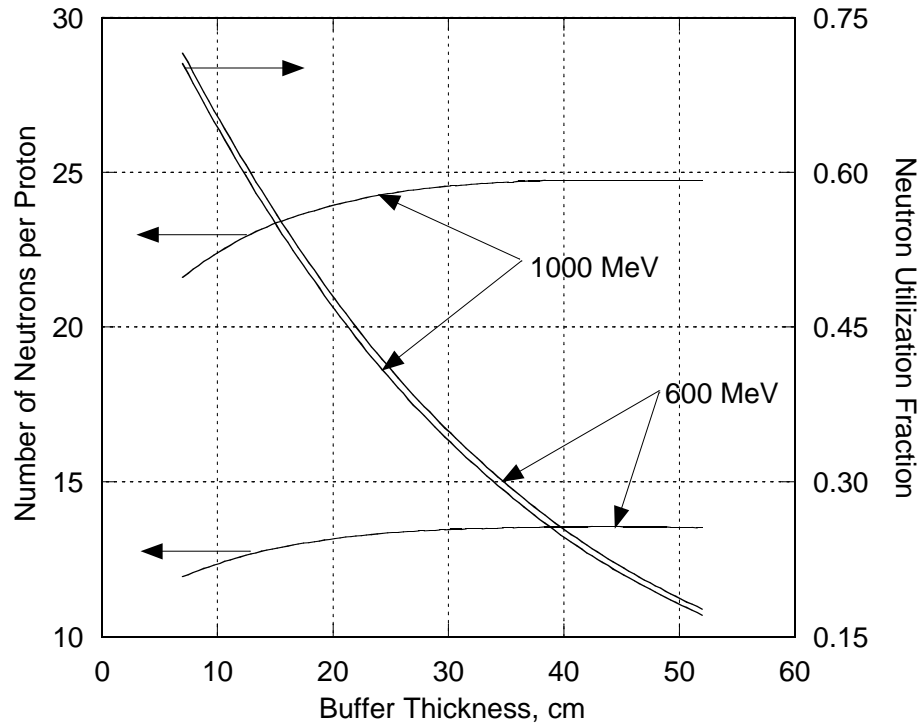


Figure 15. Neutron yield and neutron utilization fraction as a function of the buffer thickness for the lead-bismuth eutectic target with 600- and 1000-MeV proton beams

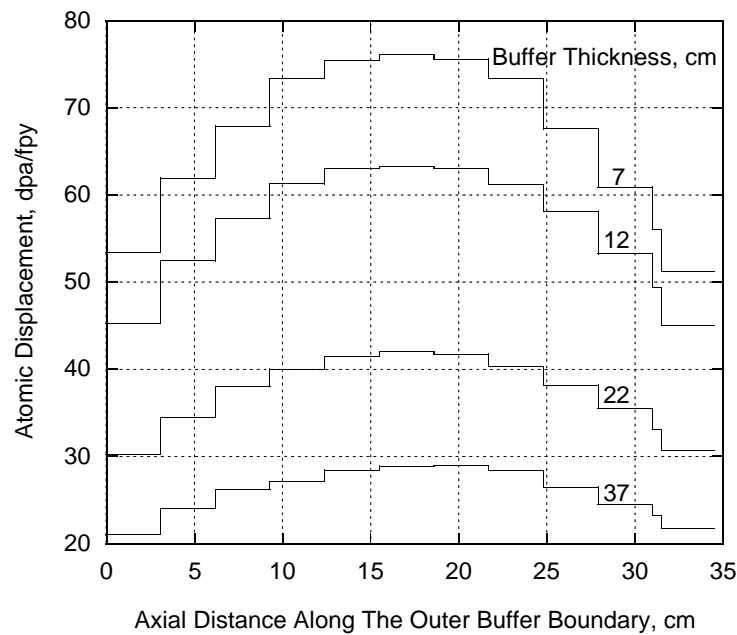


Figure 16. Atomic displacement in the structural material outside the target as a function of the distance along the outer buffer boundary measured in the beam direction for the lead-bismuth eutectic target with 600-Mev proton beam and different buffer thicknesses

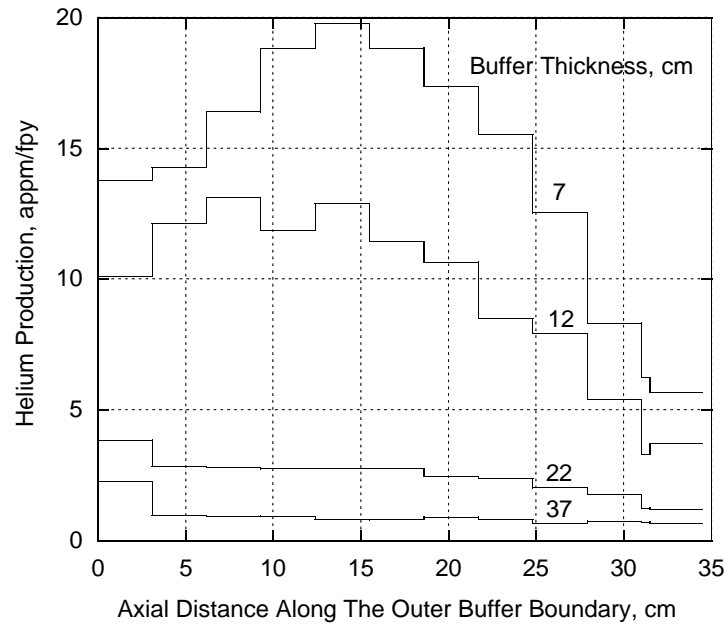


Figure 17. Helium gas production in the structural material outside the target as a function of the distance along the outer buffer boundary measured in the beam direction for the lead-bismuth eutectic target with 600-Mev proton beam and different buffer thicknesses

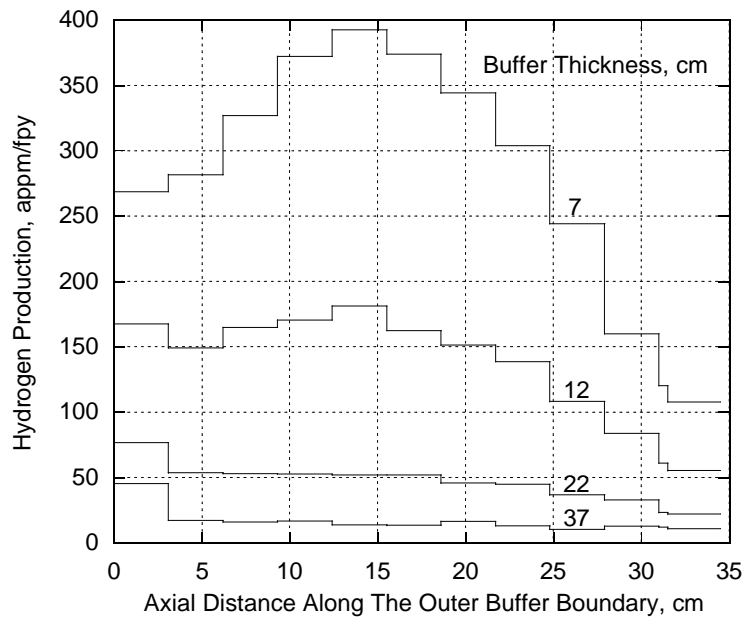


Figure 18. Hydrogen gas production in the structural material outside the target as a function of the distance along the outer buffer boundary measured in the beam direction for the lead-bismuth eutectic target with 600-Mev proton beam and different buffer thicknesses

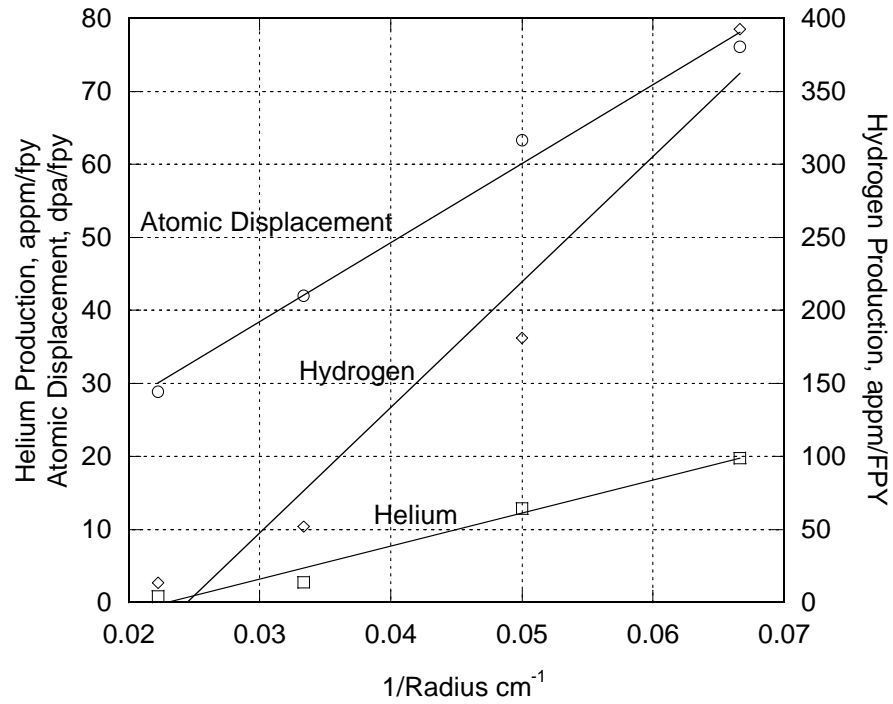


Figure 19. Midplane nuclear responses in the structural material outside the target as a function of the reciprocal of the outer buffer radius for the lead-bismuth eutectic target with 600-MeV proton beam

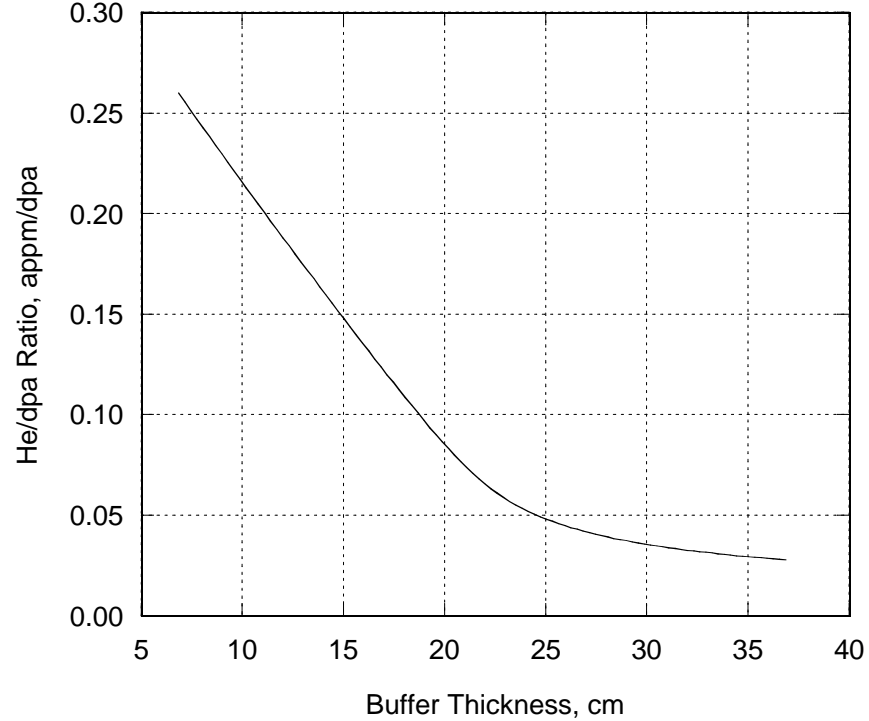


Figure 20. Helium to atomic displacement ratio in structural material outside the target as function of the buffer thickness of the lead-bismuth eutectic target with 600 MeV proton beam

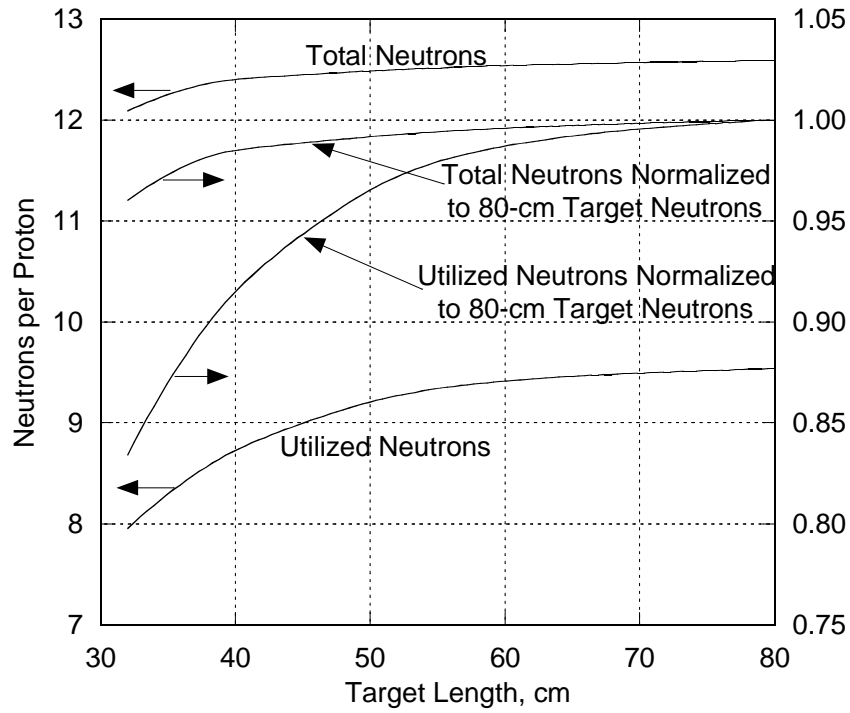


Figure 21. Number of generated and utilized neutrons per 600-MeV proton as a function of the LBE target length

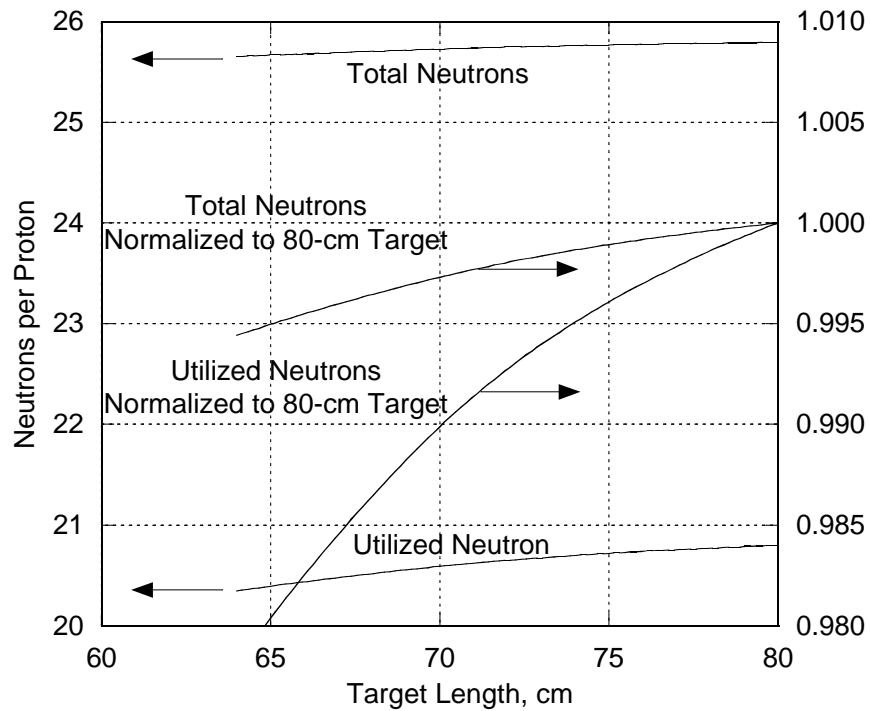


Figure 22. Number of generated and utilized neutrons per 1000-MeV proton as a function of the LBE target length

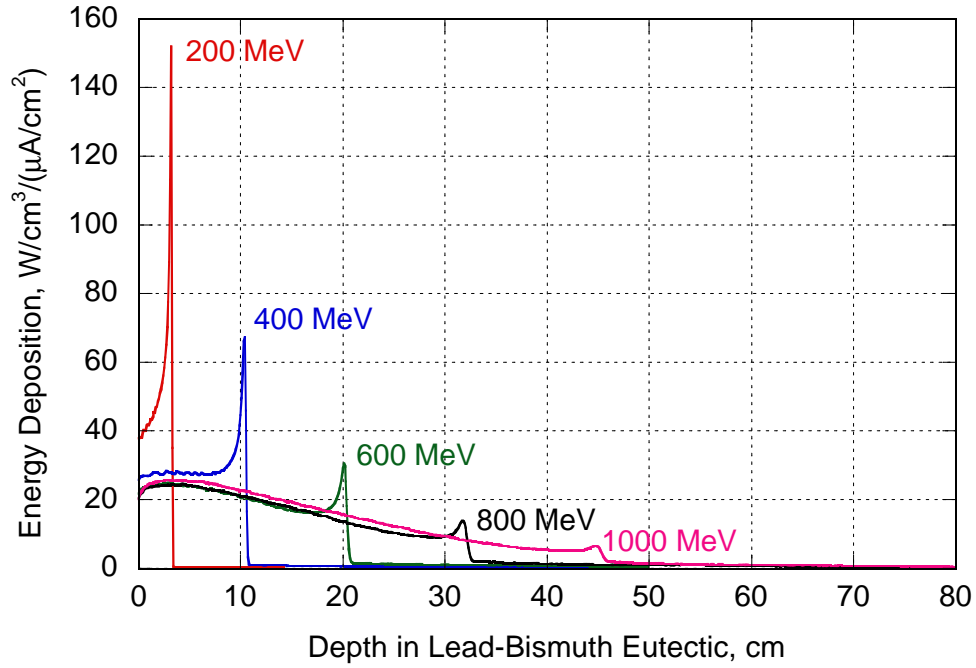


Figure 23. Spatial energy deposition in the lead-bismuth eutectic for different deuteron energies with a uniform beam distribution normalized to the deuteron beam current density

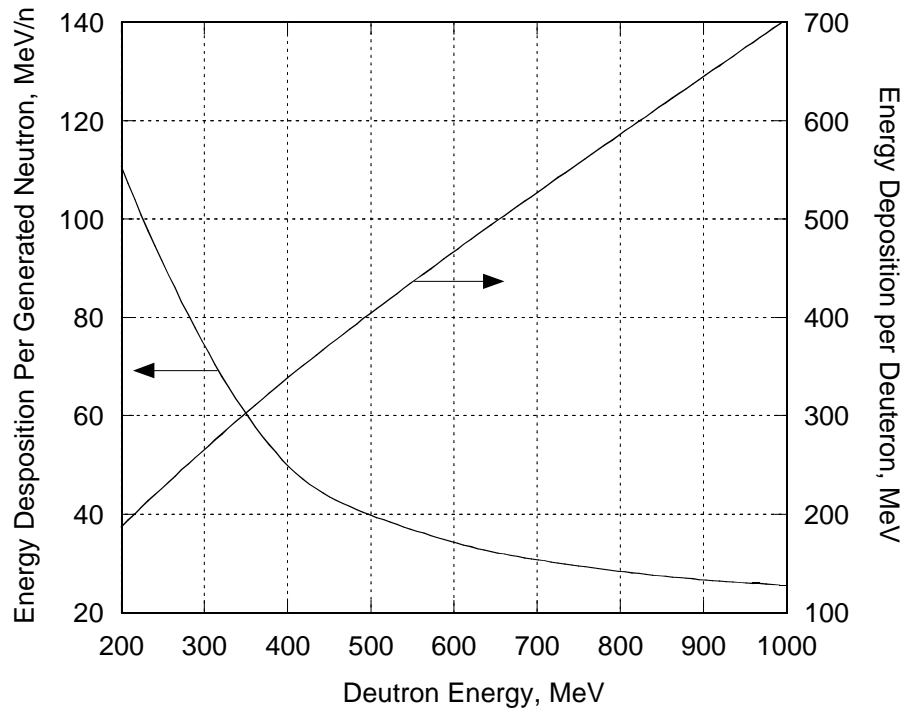


Figure 24. Energy deposition in the lead-bismuth eutectic as a function of the deuteron energy normalized per incident deuteron on the right axis and per generated neutron on the left axis

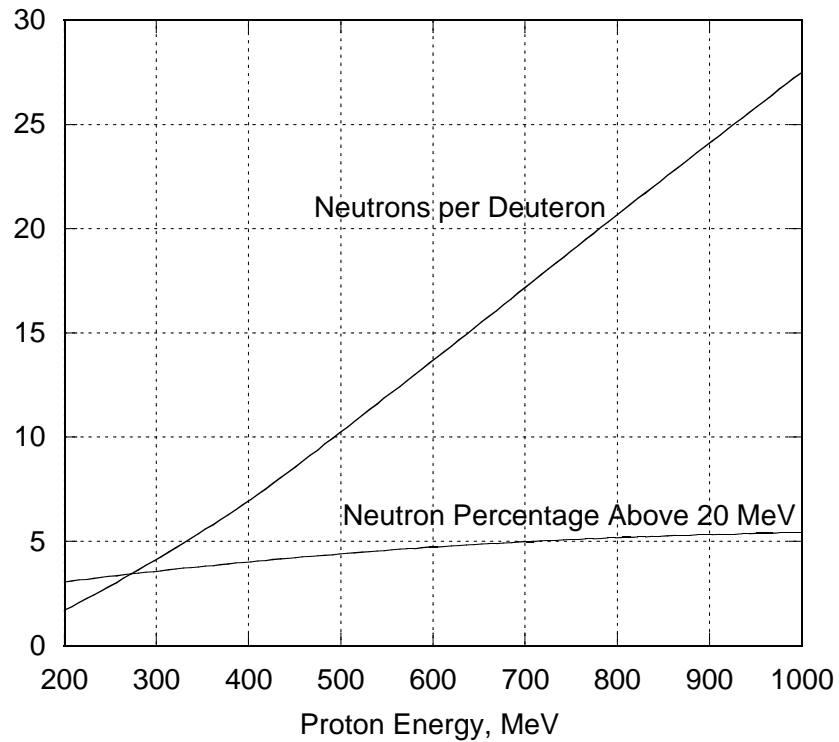


Figure 25. Number of neutrons per deuteron and neutron percentage with energy above 20 MeV as a function of the deuteron energy from the lead-bismuth eutectic

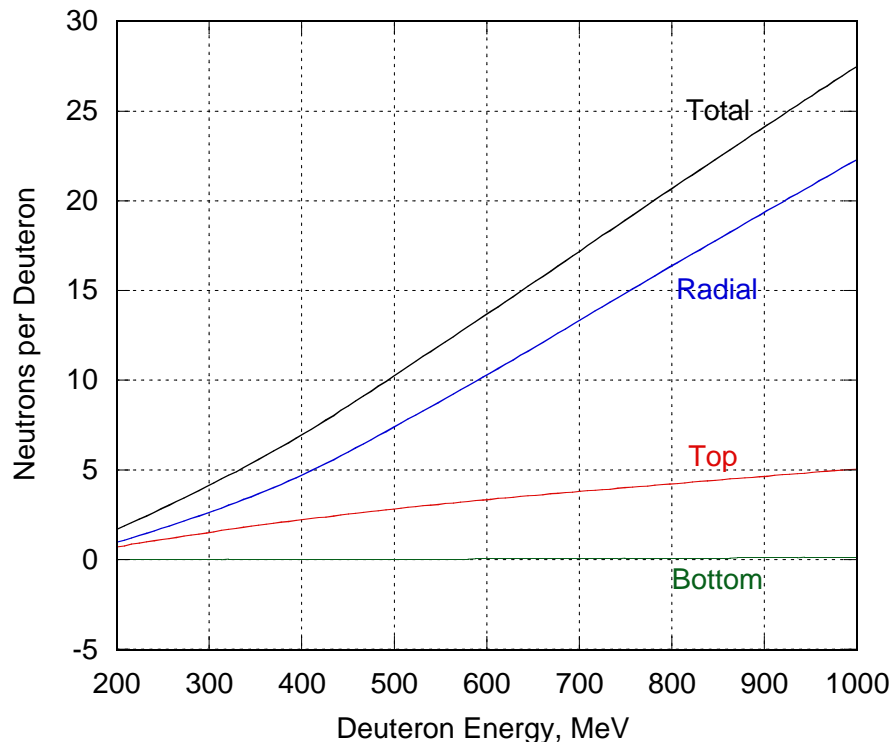


Figure 26. Number of neutrons per deuteron leaving the lead-bismuth eutectic target boundaries as a function of the deuteron energy

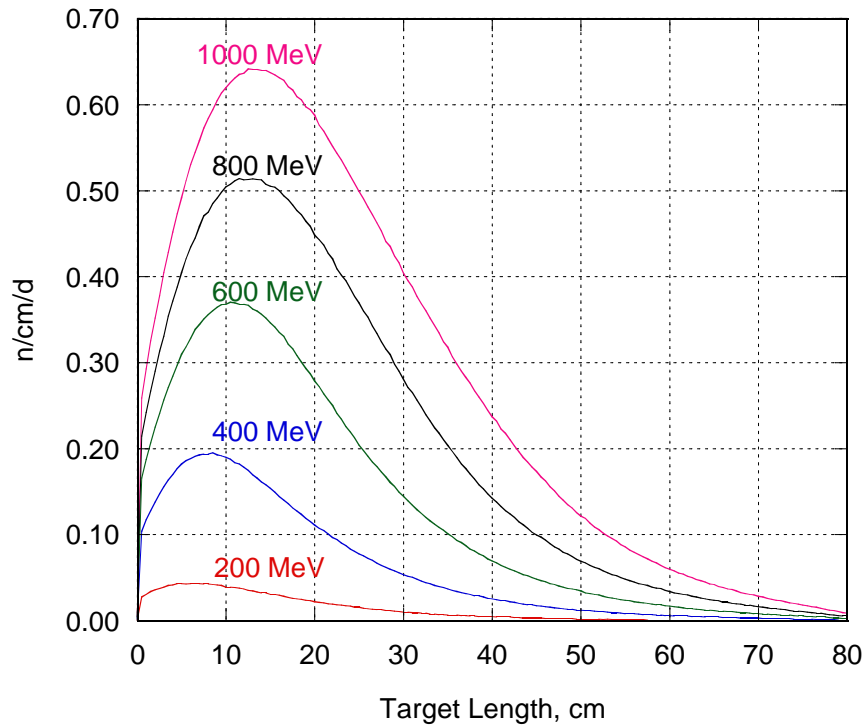


Figure 27. Generated neutron distribution along the target buffer outer surface for different deuteron energies normalized per deuteron from the lead-bismuth eutectic

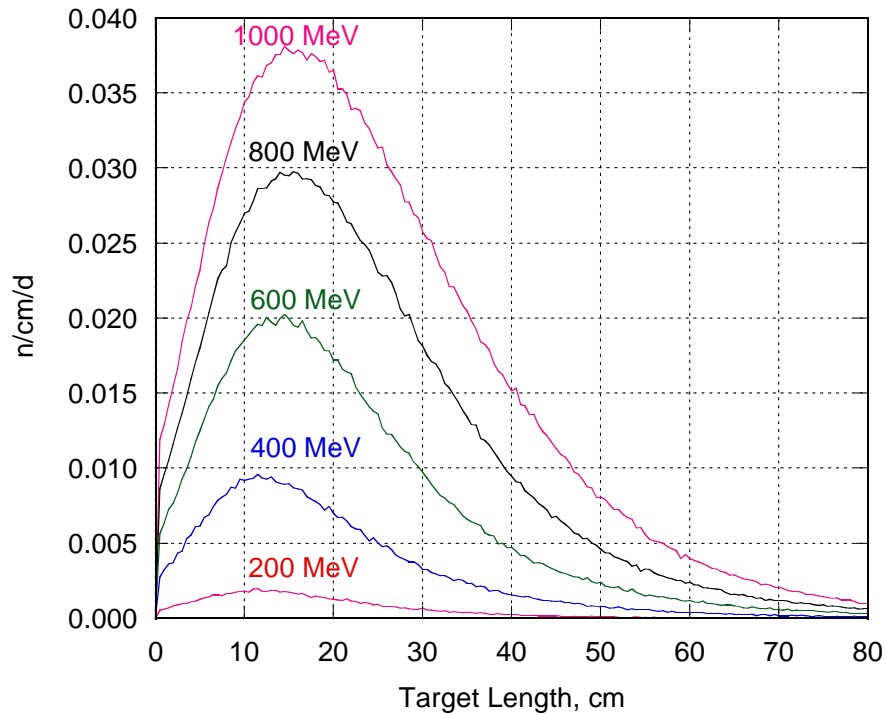


Figure 28. Generated high-energy ($E > 20$ MeV) neutron distribution along the target buffer outer surface for different deuteron energies normalized per deuteron from the lead-bismuth eutectic

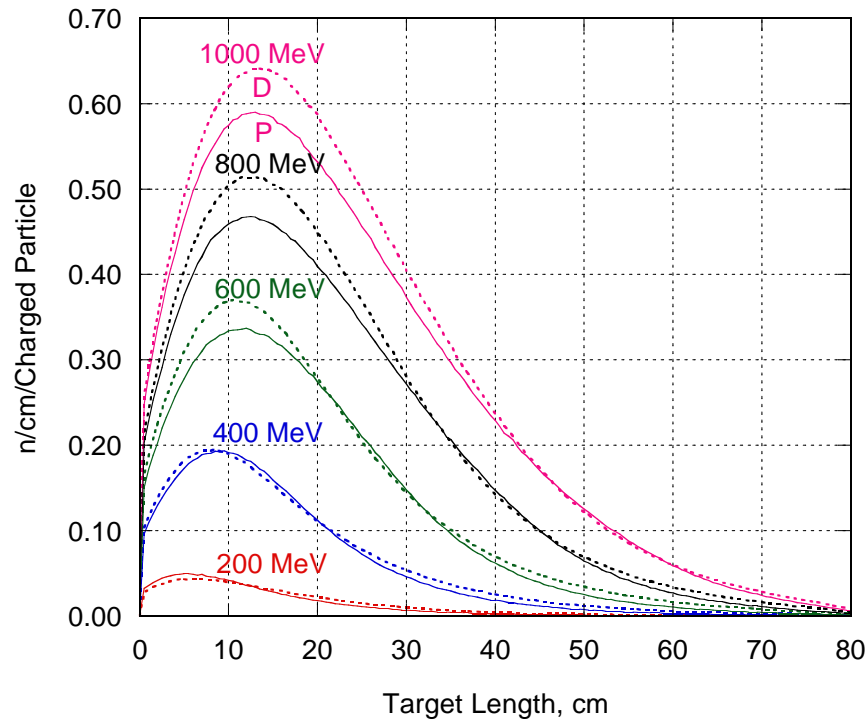


Figure 29. Generated neutron distribution along the target buffer outer surface for different proton and deuteron energies normalized per proton or deuteron from the lead-bismuth eutectic

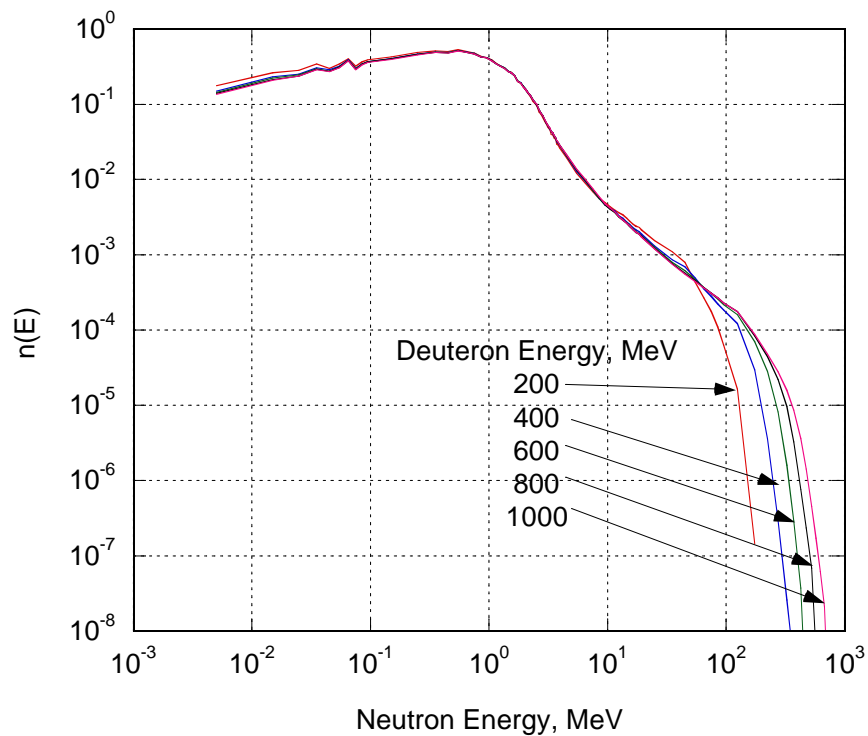


Figure 30. Generated neutron spectra for different deuteron energies normalized per generated neutron from the lead-bismuth eutectic

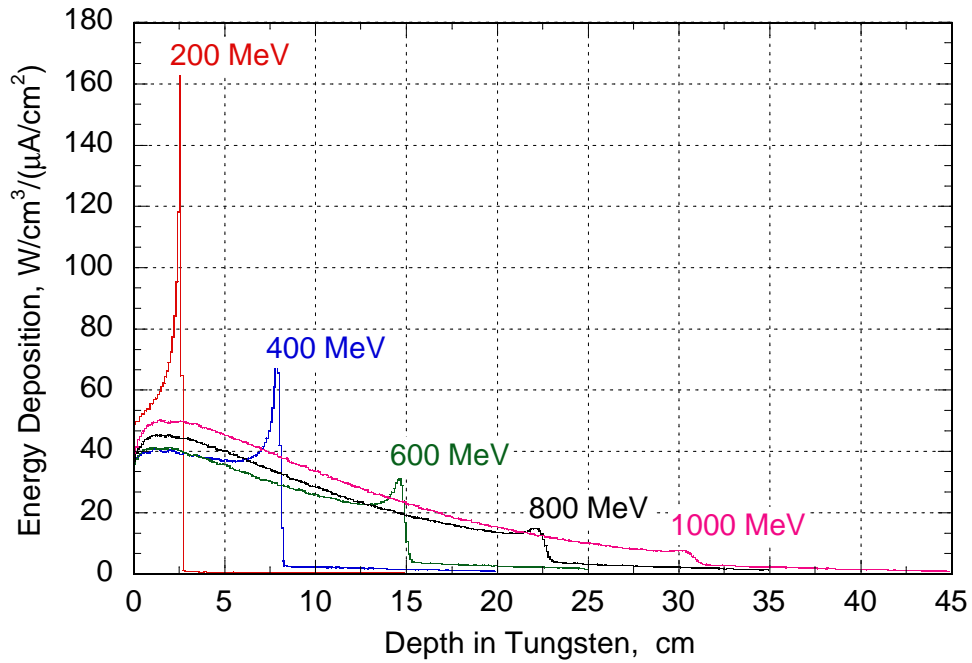


Figure 31. Spatial energy deposition in the tungsten material for different proton energies with a uniform beam distribution normalized to the proton beam current density

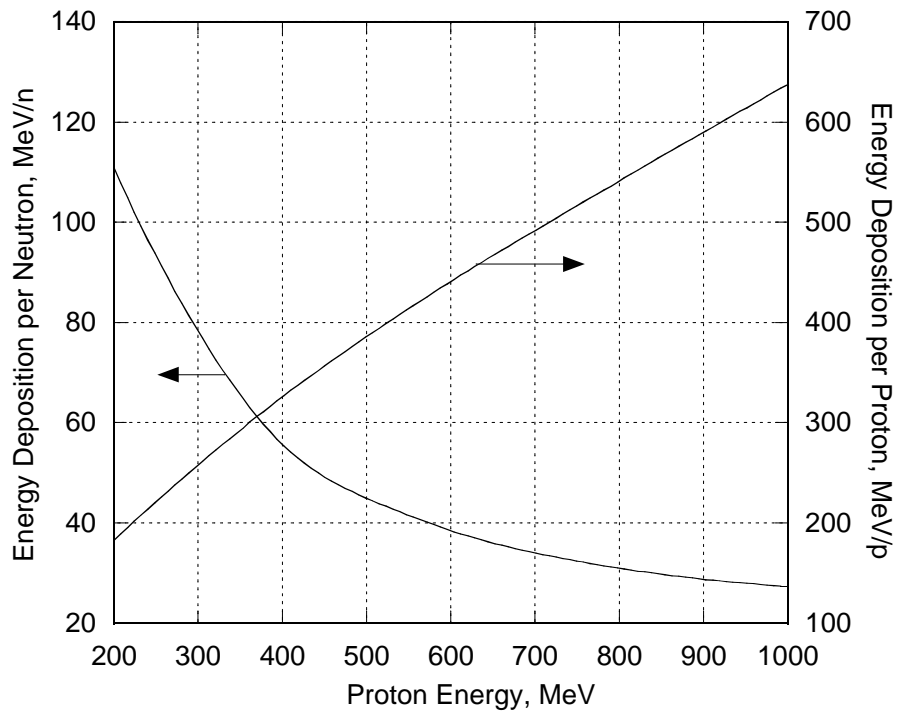


Figure 32. Energy deposition in the tungsten material as a function of the proton energy normalized per incident proton on the right axis and per generated neutron on the left axis

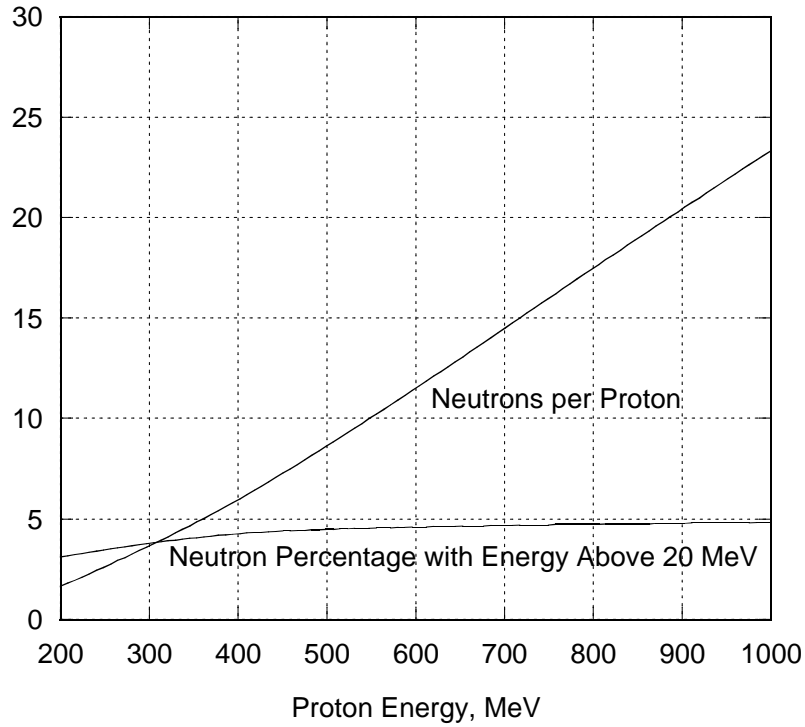


Figure 33. Number of neutrons per proton and neutron percentage with energy above 20 MeV as a function of the proton energy from the tungsten material

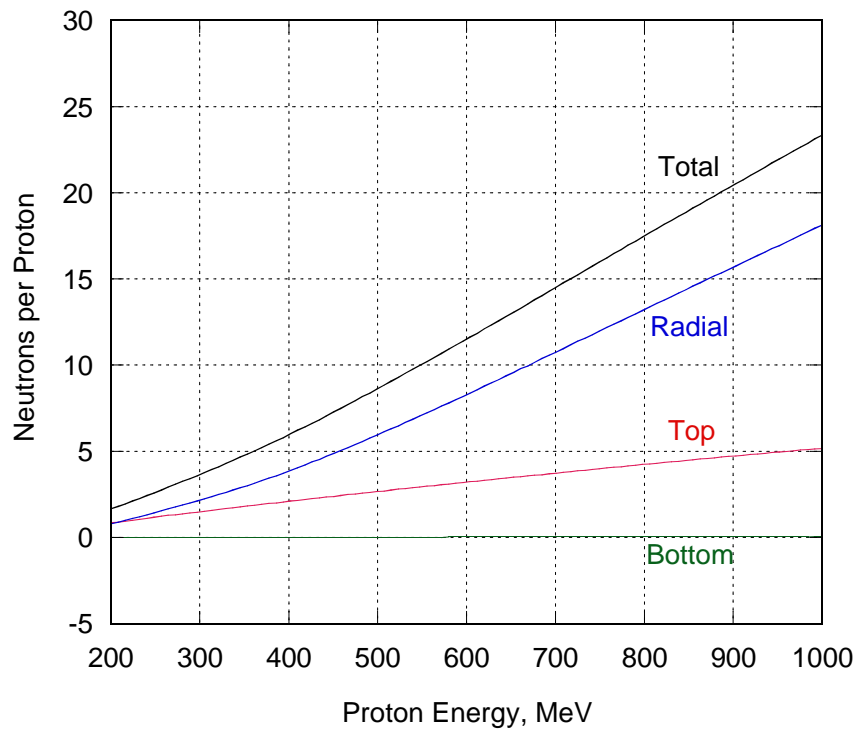


Figure 34. Number of neutrons per proton leaving the tungsten material target boundaries as a function of the proton energy

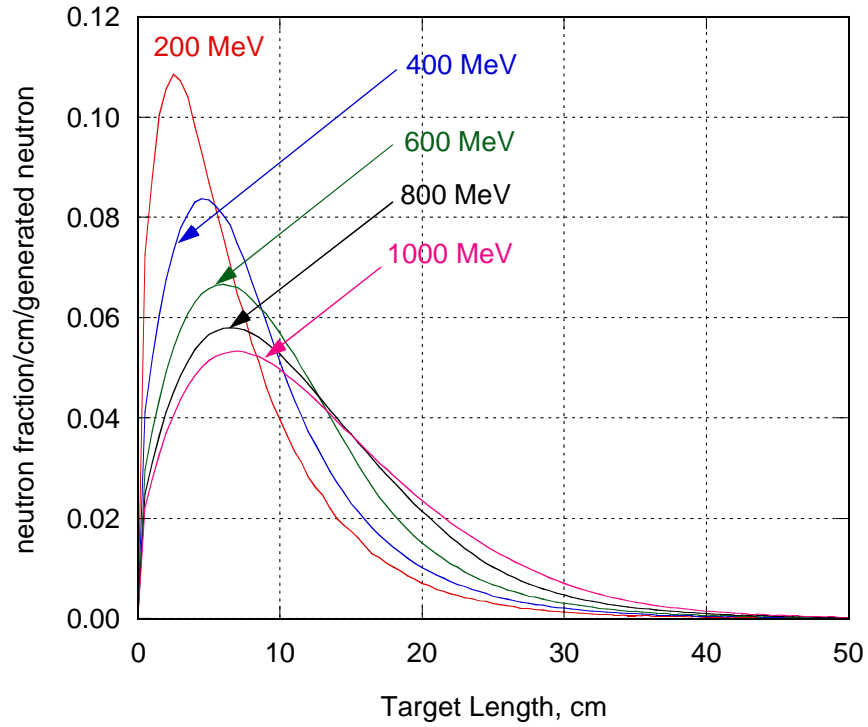


Figure 35. Generated neutron distribution along the target buffer outer surface for different proton energies normalized per generated neutron from the tungsten material

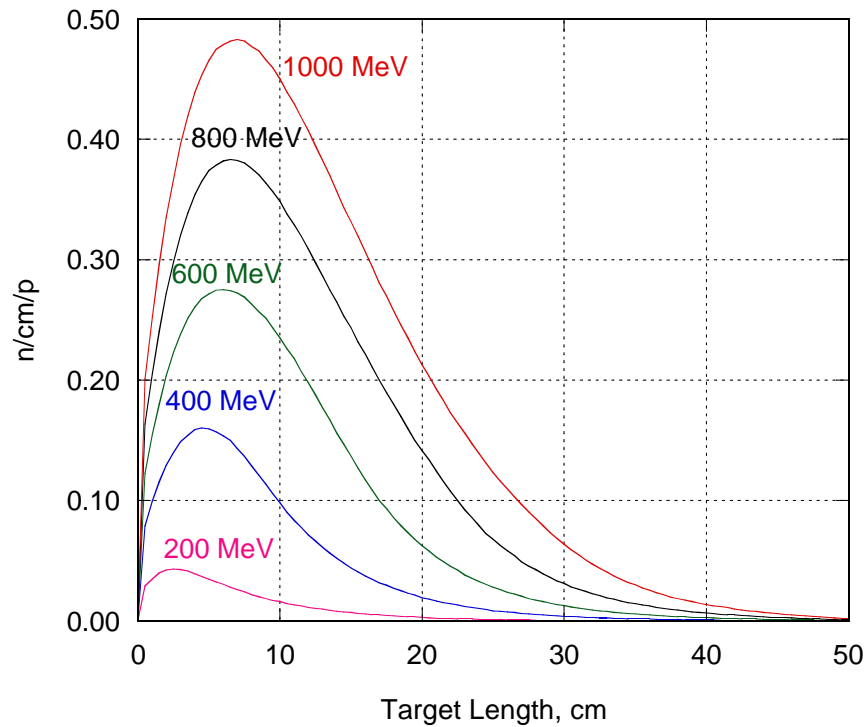


Figure 36. Generated neutron distribution along the target buffer outer surface for different proton energies normalized per proton from the tungsten material

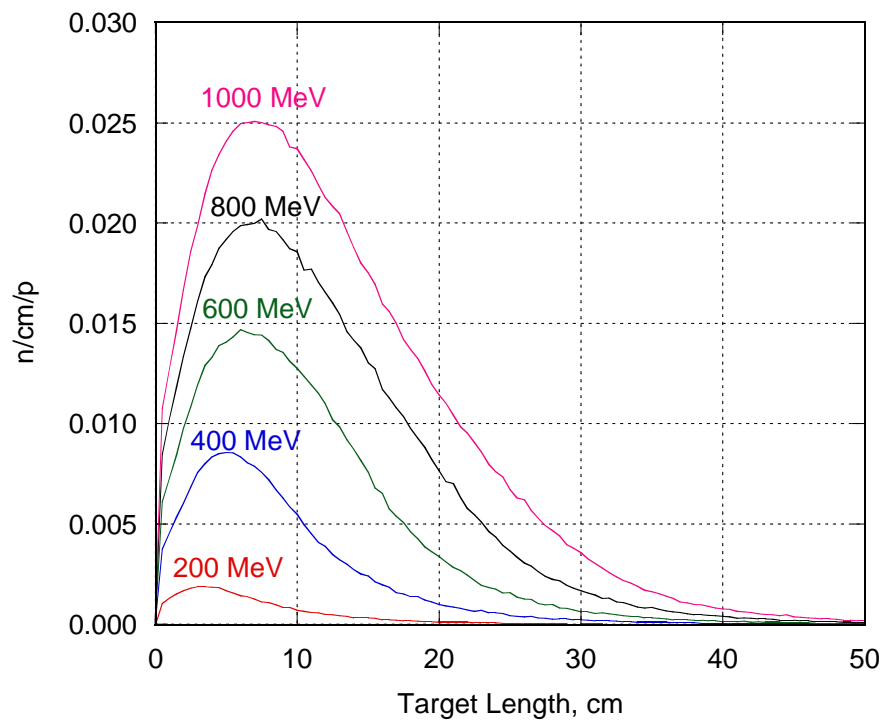


Figure 37. Generated high-energy ($E > 20$ MeV) neutron distribution along the target buffer outer surface for different proton energies normalized per proton from the tungsten material

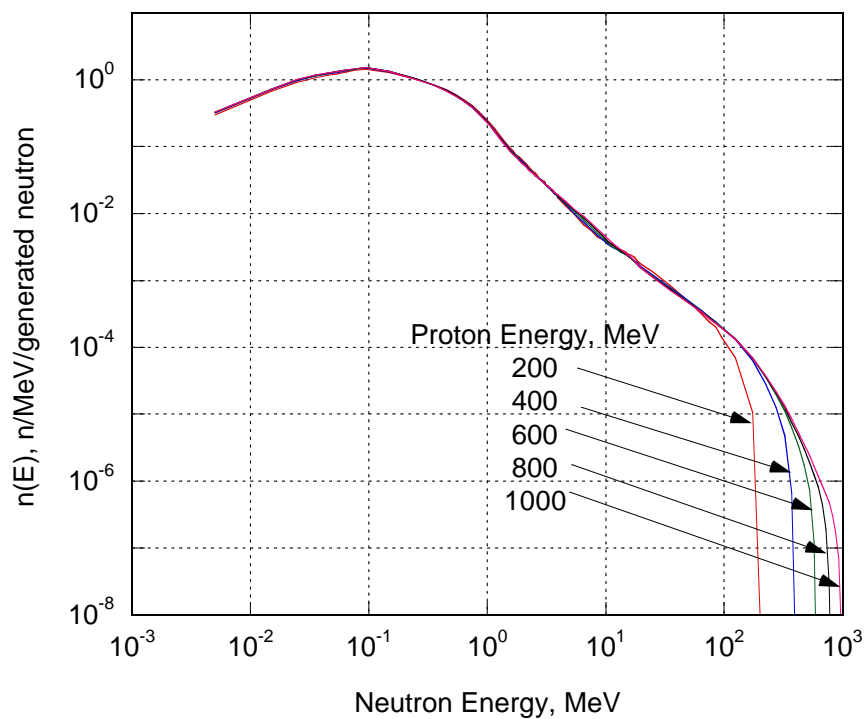


Figure 38. Generated neutron spectra for different proton energies normalized per generated neutron from the tungsten material

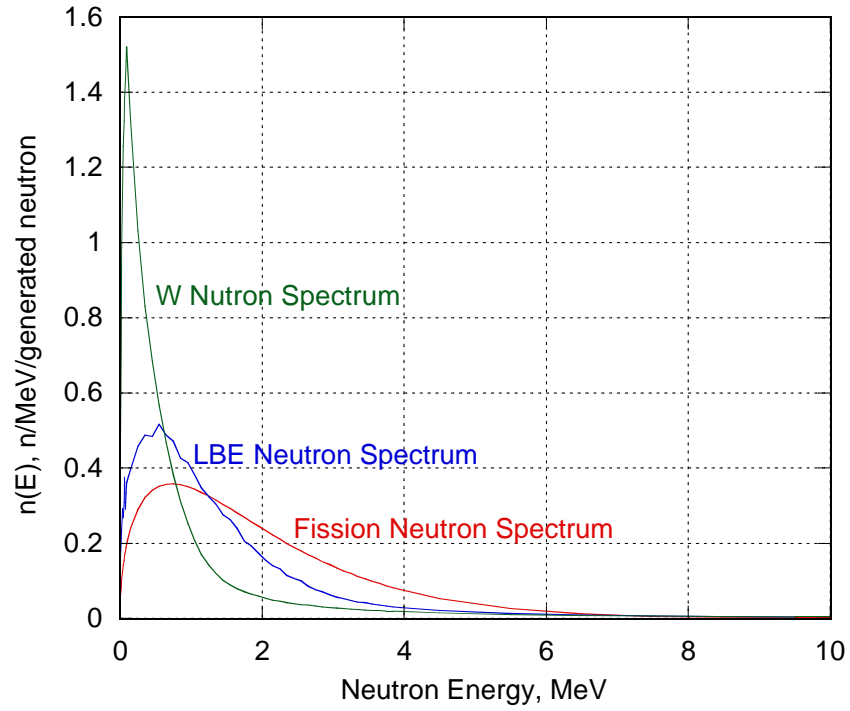


Figure 39. Fission neutron spectrum compared to the neutron spectrum from the lead-bismuth eutectic and the tungsten material generated by proton normalized per neutron

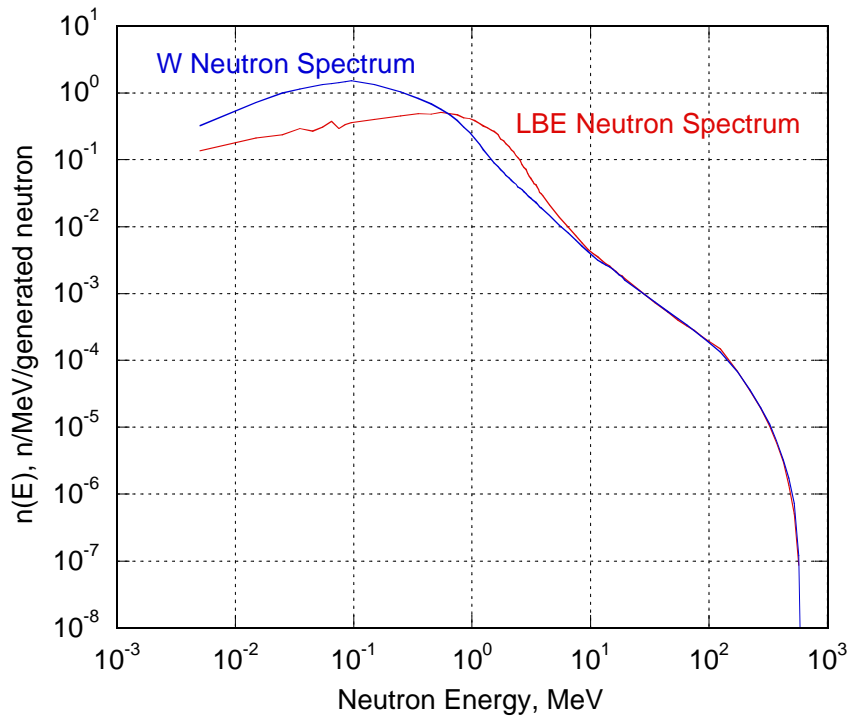


Figure 40. Neutron spectra from the lead-bismuth eutectic and the tungsten material generated by proton normalized per neutron

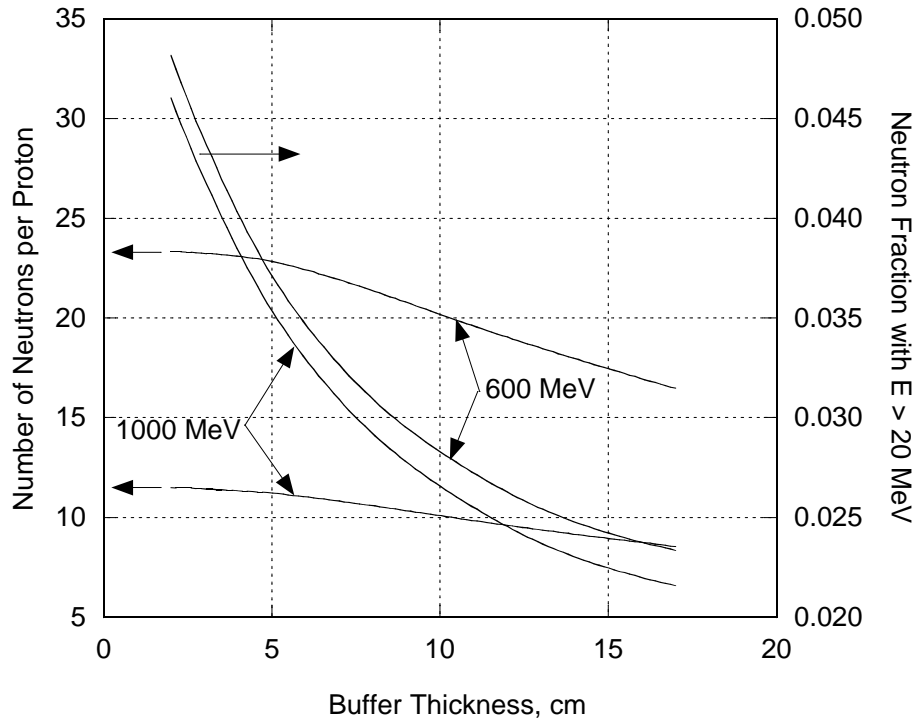


Figure 41. Number of generated neutrons per proton as a function of the buffer thickness from the tungsten material for different proton energies

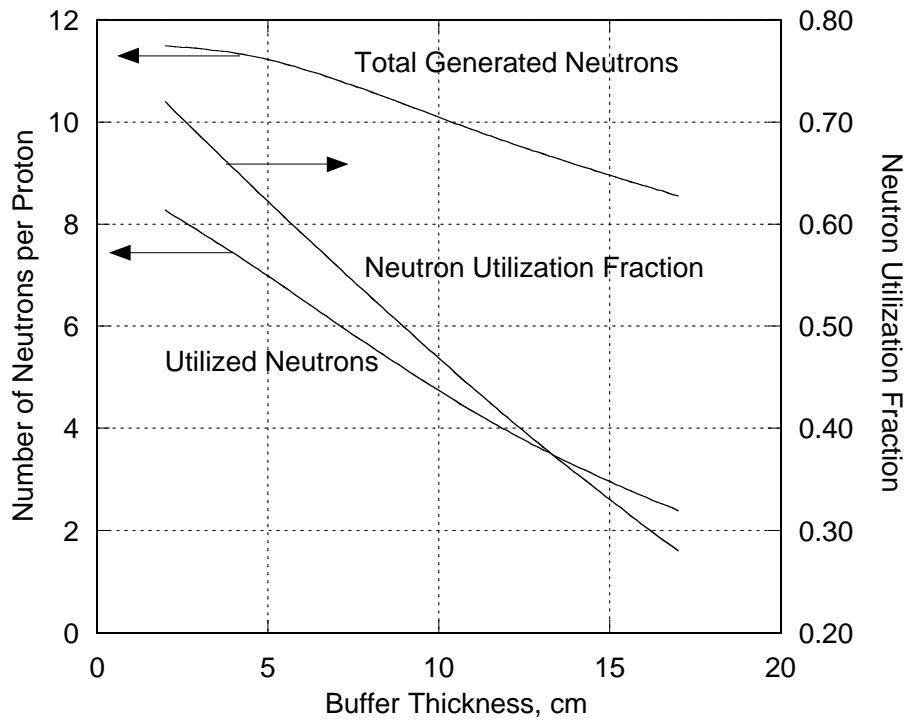


Figure 42. Neutron yield and neutron utilization as a function of the buffer size for the tungsten material with 600-MeV proton beam

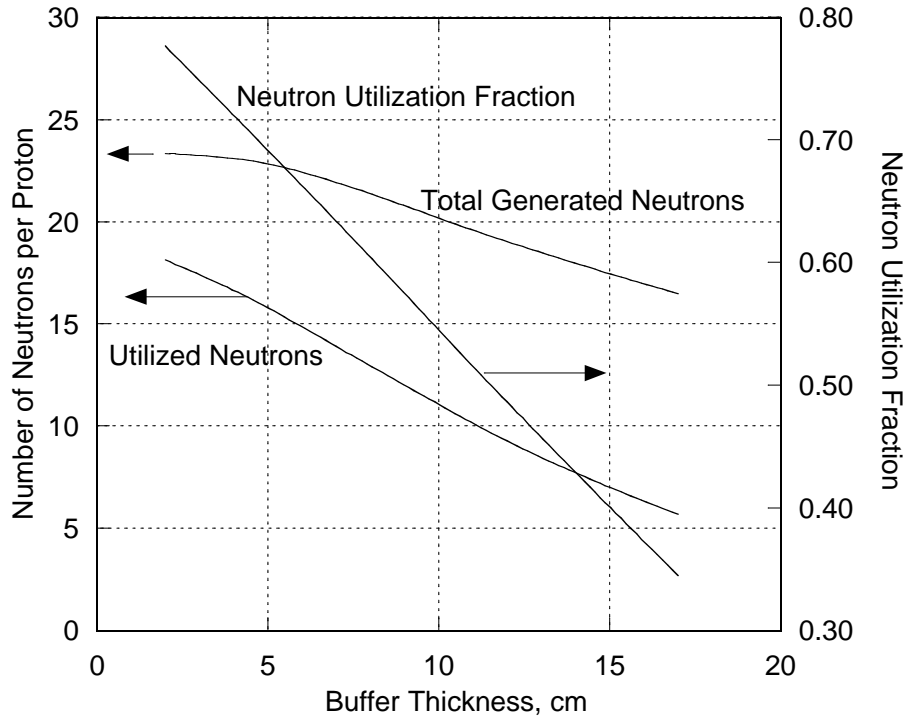


Figure 43. Neutron yield and neutron utilization as a function of the buffer size for the tungsten material with 1000-MeV proton beam

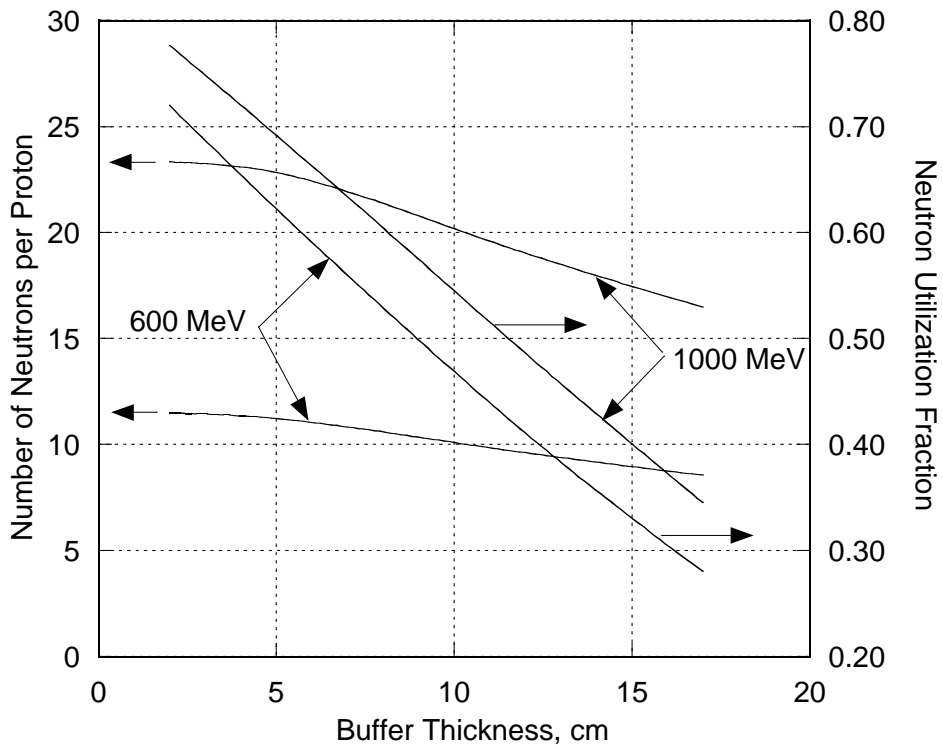


Figure 44. Neutron yield and neutron utilization fraction as a function of the buffer thickness for the tungsten material with 600- and 1000-MeV proton beams

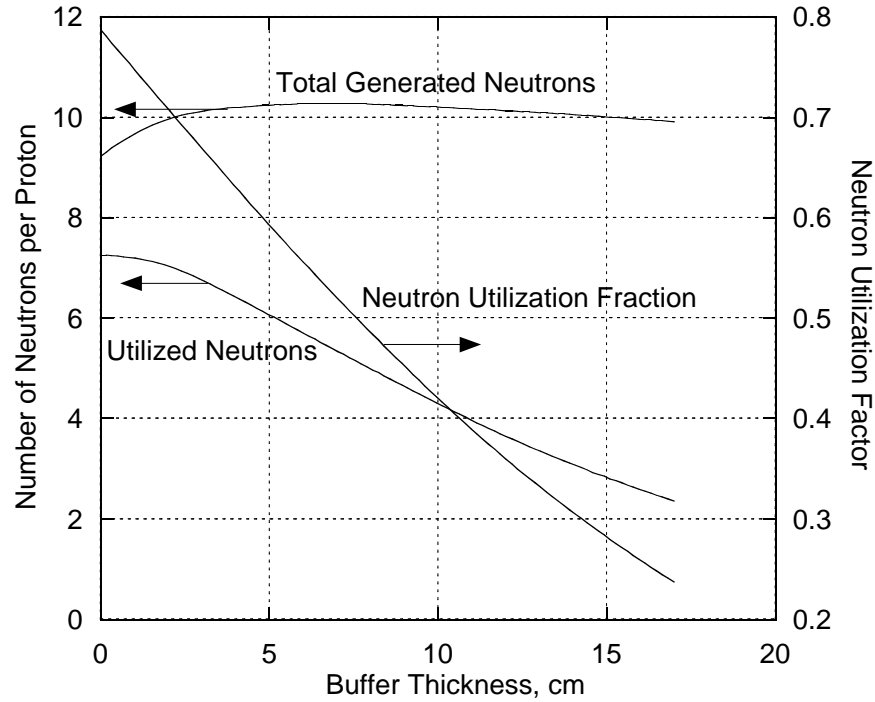


Figure 45. Number of generated neutrons per proton as a function of the buffer thickness for the sodium-cooled tungsten target with the 600-MeV proton beam

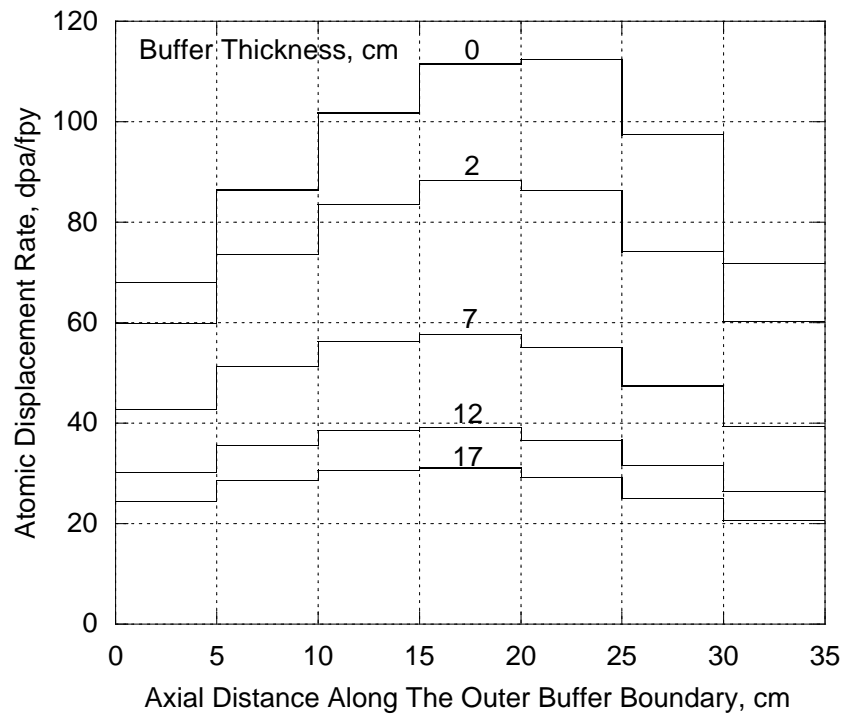


Figure 46. Atomic displacement in the structural material outside the target as a function of the distance along the outer buffer boundary measured in the beam direction for the sodium-cooled tungsten target with 600-MeV proton beam and different buffer thicknesses

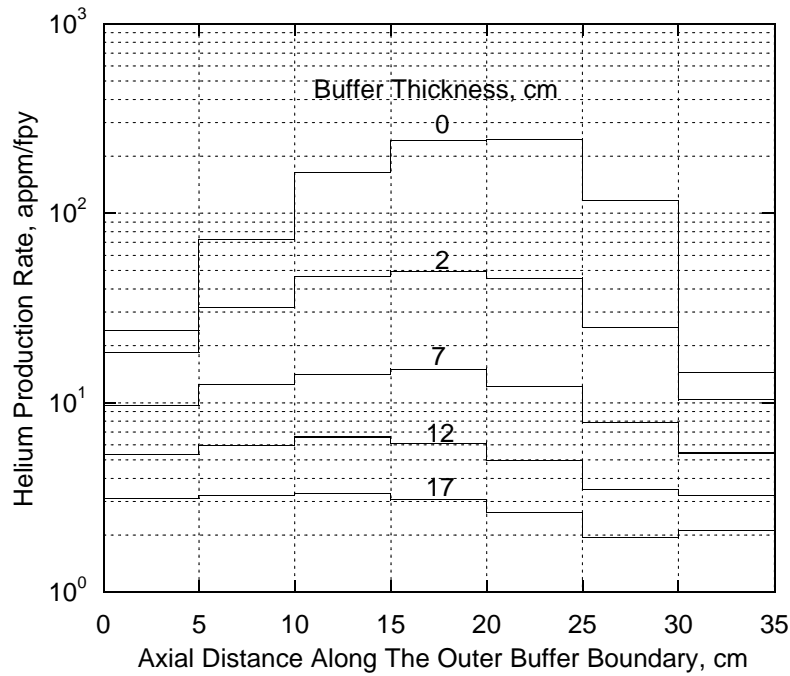


Figure 47. Helium gas production in the structural material outside the target as a function of the distance along the outer buffer boundary measured in the beam direction for the sodium-cooled tungsten target with 600-Mev proton beam and different buffer thicknesses

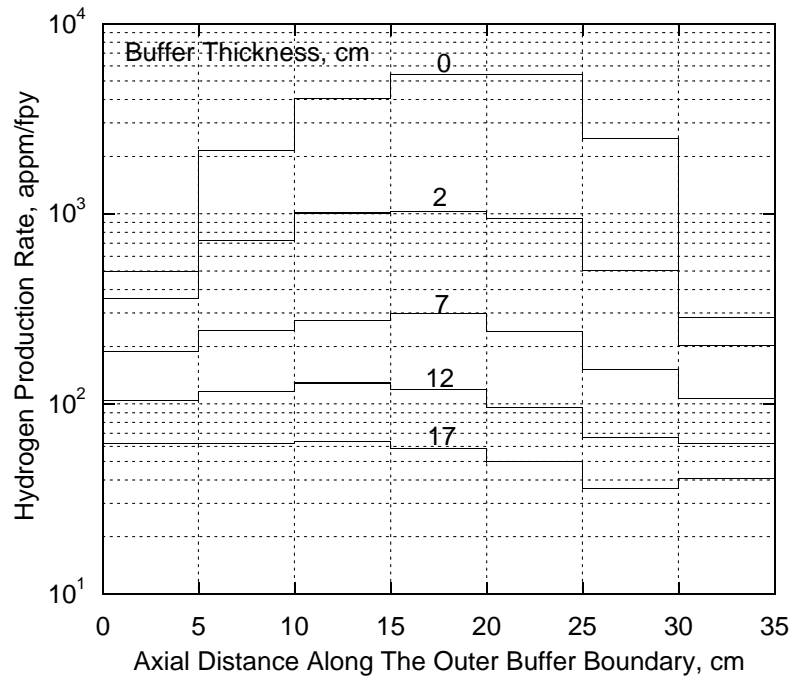


Figure 48. Hydrogen gas production in the structural material outside the target as a function of the distance along the outer buffer boundary measured in the beam direction for the sodium-cooled tungsten target with 600-Mev proton beam and different buffer thicknesses

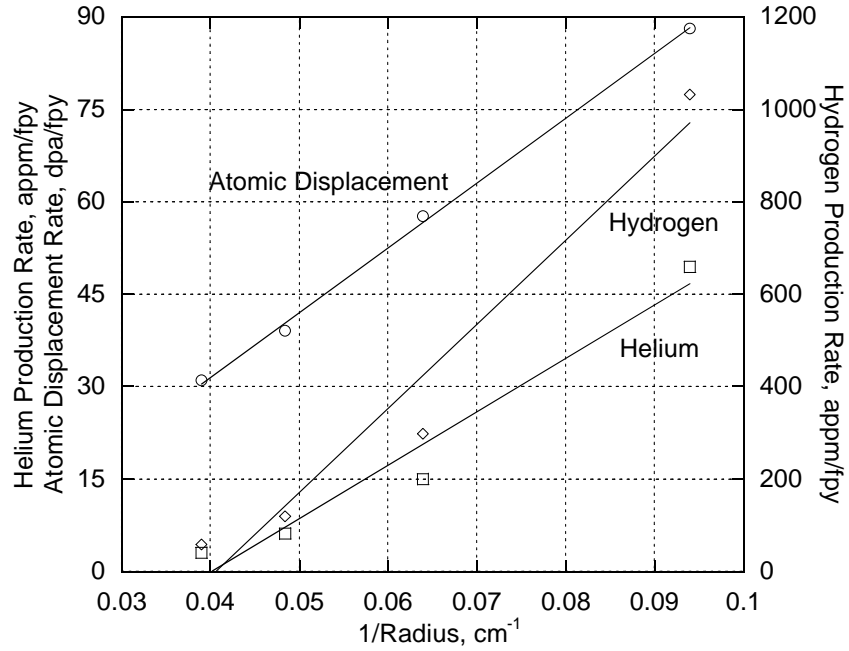


Figure 49. Midplane nuclear responses in the structural material outside the target as a function of the reciprocal of the outer buffer radius for the sodium-cooled tungsten target with 600-MeV proton beam

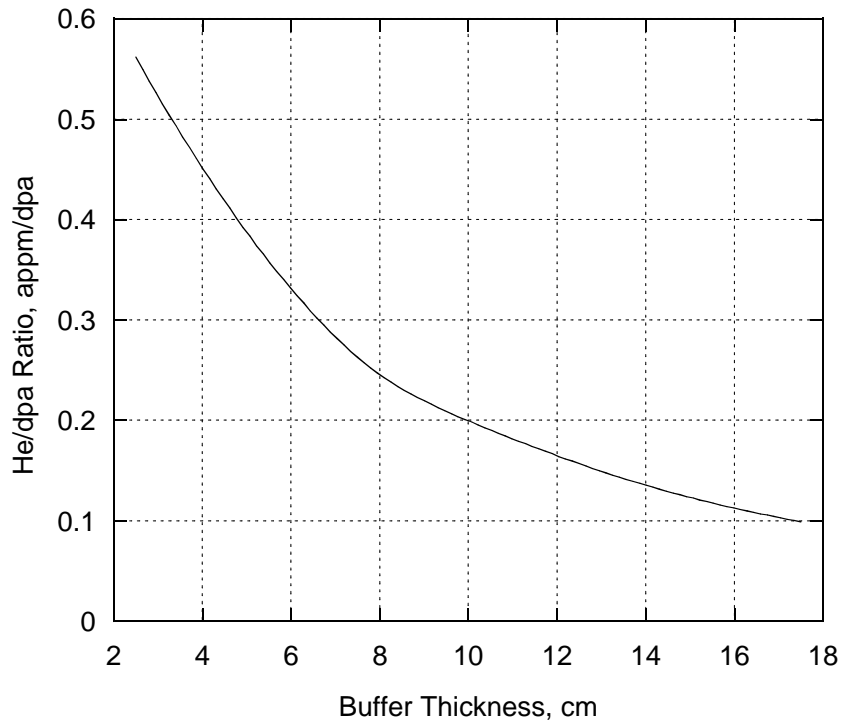


Figure 50. Helium to atomic displacement ratio in structural material outside the target as function of the buffer thickness of the sodium-cooled tungsten target with 600 MeV proton beam

Table 1. Target window nuclear responses from 600 MeV proton beam with 40 $\mu\text{A}/\text{cm}^2$ current density of the lead-bismuth target concept

Energy deposition, W/cm^3	766.49
Atomic displacement, dpa/y	
Neutrons	46.2
Protons	21.1
Total	67.3
Helium production, appm/fpy	
Low energy neutrons = 20 MeV	5.7
High energy neutrons > 20 MeV	50.2
Protons	1437.3
Total	1493.2
Hydrogen production, appm/fpy	
Low energy neutrons = 20 MeV	6.3
High energy neutrons > 20 MeV	1010.1
Protons	26753.1
Total	27769.5

DISTRIBUTION LIST FOR ANL/TD/02-02

Internal

R. K. Ahluwalia	J. Herceg	C. Reed
S. K. Bhattacharyya	R. Hill	J. Roglans
M. Billone	H. Khalil	T. Taiwo
J. Brooks	J. Laidler	R. Valentin
J. Cahalan	J. Liaw	D. Wade
D. Crawford	S. Majumdar	D. Weber
D. Ehst	V. Maroni	R. W. Weeks
P. Finck	R. McKnight	M. Williamson
E. Fujita	K. Natesan	
Y. Gohar (10)	B. Picologlou	

External

ANL-E Library
ANL-W Library
DOE/OSTI (2)
H. A. Abderrahim, SCK-CEN, Belgium
E. Adamov, Research and Development Institute of Power Engineering, Moscow, Russia
J. Anderson, Los Alamos National Laboratory, Los Alamos, NM
E. Arther, Los Alamos National Laboratory, Los Alamos, NM
R. Aymar, ITER Garching, Garching, Germany
C. Baker, University of California, San Diego, CA
D. Baldwin, General Atomic, San Diego, CA
C. G. Bathke, Los Alamos National Laboratory, Los Alamos, NM
G. Bauer, Forschungszentrum Juelich, Germany
A. Baxter, General Atomics, San Diego, CA
D. Beller, Harry Reid Center for Environmental Studies, Las Vegas, NV
G. Benamati, ENEA, Italy
D. R. Bennett, Los Alamos National Laboratory, Los Alamos, NM
S. Berk, U.S. Department of Energy, Germantown, MD
E. E. Bloom, Oak Ridge National Laboratory, Oak Ridge, TN
C. Bolton, U.S. Department of Energy, Germantown, MD
M. Cappiello, Los Alamos National Laboratory, Los Alamos, NM
E. Cheng, TSI Research Inc., San Diego, CA
X. Cheng, Forschungszentrum Karlsruhe, Germany
V. Chernov, Bochvar Research Institute of Inorganic Materials, Moscow, Russia
V. Chuyanov, ITER Garching, Garching, Germany
R. Dagazian, U.S. Department of Energy, Germantown, MD
J. Davis, The Boeing Company, St. Louis, MO

W. Dove, U.S. Department of Energy, Germantown, MD
M. Eid, CEA, Gif-sur-Yvette, France
L. El-Guebaly, University of Wisconsin, Madison, WI
G. Emmert, University of Wisconsin, Madison, WI
V. Evtikhin, State Enterprise Red Star, Moscow, Russia
O. Filatov, Efremov Scientific Research Institute, St. Petersburg, Russia
U. Fischer, Forschungszentrum Karlsruhe, Germany
M. Fuetterer, CEA, Gif-sur-Yvette, France
T. Gabriel, Oak Ridge National Laboratory, Oak Ridge, TN
M. Gasparotto, ENEA, Frascati, Italy
W. Gauster, Sandia National Laboratories, Albuquerque, NM
L. Giancarli, CEA, Gif-sur-Yvette, France
J. Gilleland, Archimedes Technology Group, Inc., San Diego, CA
F. Goldner, U.S. Department of Energy, Germantown, MD
R. Goldston, Princeton Plasma Physics Laboratory, Princeton, NJ
D. Gorse, CNRS-CECM, France
F. Groeschel, PSI, Switzerland
J. Gulliford, AEA Technology, United Kingdom
W. G. Halsely, Los Alamos National Laboratory, Los Alamos, NM
J. Herczeg, U.S. Department of Energy, Washington, DC
G. Heusener, Forschungszentrum Karlsruhe, Karlsruhe, Germany
M. Kawai, KEK, Japan
H. Kawamura, Japan Atomic Energy Research Institute, Oarai, Japan
K. Kikuchi, JEARI, Japan
T. Kirchner, SUBATECH, France
V. Kirillov, Efremov Scientific Research Institute, St. Petersburg, Russia
J. U. Knebel, Forschungszentrum Karlsruhe, Karlsruhe, Germany
R. A. Krakowski, Los Alamos National Laboratory, Los Alamos, NM
G. Kulcinski, University of Wisconsin, Madison, WI
I. Lyublinski, State Enterprise Red Star, Moscow, Russia
H. Maekawa, Japan Atomic Energy Research Institute, Japan
S. Malang, Forschungszentrum Karlsruhe, Karlsruhe, Germany
S. Maloy, Los Alamos National Laboratory, Los Alamos, NM
D. Markovskij, Kurchatov Institute, Moscow, Russia
W. Marton, U.S. Department of Energy, Germantown, MD
Y. Martynenko, Kurchatov Institute, Moscow, Russia
R. Matera, URC-IHCP, Ispra, Italy
S. Matsuda, Japan Atomic Energy Research Institute, Naka, Japan
B. Matthews, Los Alamos National Laboratory, Los Alamos, NM
K. McCarthy, Idaho National Engineering and Environmental Laboratory, Idaho Falls, ID
R. Miller, University of California, San Diego, CA
F. Najmabadi, University of California, San Diego, CA
R. Nygren, Sandia National Laboratories, Albuquerque, NM
A. Opdenaker, U.S. Department of Energy, Germantown, MD
R. Parker, Massachusetts Institute of Technology, Cambridge, MA
K. Pasamehmetoglu, Los Alamos National Laboratory, Los Alamos, NM
J. Perkins, Lawrence Livermore National Laboratory, Livermore, CA

D. Petti, Idaho National Engineering and Environmental Laboratory, Idaho Falls, ID
 S. Piet, Idaho National Engineering and Environmental Laboratory, Idaho Falls, ID
 E. J. Pitcher, Los Alamos National Laboratory, Los Alamos, NM
 D. Post, Lawrence Livermore National Laboratory, Livermore, CA
 J. Raeder, ITER Garching, Garching, Germany
 C. Rodriguez, General Atomics, San Diego, CA
 M. Salvatores, CEA Cadarache, France
 M. Sawan, University of Wisconsin, Madison, WI
 F. Scaffidi-Argentina, EFDA Close Support Unit, Culham Science Centre, UK
 T. Schulenberg, Forschungszentrum Karlsruhe, Karlsruhe, Germany
 K. Schultz, General Atomic, San Diego, CA
 T. Shannon, University of Tennessee, Knoxville, TN
 G. Shatalov, Kurchatov Institute of Atomic Energy, Moscow, Russia
 R. Sheffield, Los Alamos National Laboratory, Los Alamos, NM
 Yu. A. Sokolov, Ministry of Atomic Power, Moscow, Russia
 M. Solonin, Bochvar Research Institute of Inorganic Materials, Moscow, Russia
 W. M. Stacey, Georgia Institute of Technology, Atlanta, GA
 D. Steiner, Rensselaer Polytechnic Institute, Troy, NY
 Y. Strebkov, Research and Development Institute of Power Engineering, Moscow, Russia
 K. Sumita, Osaka University, Osaka, Japan
 I. Sviatoslavsky, University of Wisconsin, Madison, WI
 A Takahashi, Osaka University, Osaka, Japan
 H. Takatsu, Japan Atomic Energy Research Institute, Tokyo, Japan
 D. Thome, General Atomic, San Diego, CA
 M. Tillack, University of California, San Diego, CA
 M. Todosow, Brookhaven National Laboratory, Upton, L.I., NY
 H. Trellue, Los Alamos National Laboratory, Los Alamos, NM
 J. Van der Laan, NRG Petten, Petten, The Netherlands
 E. P. Velikov, Kurchatov Institute of Atomic Energy, Moscow, Russia
 L. Waters, Los Alamos National Laboratory, Los Alamos, NM
 C. Wong, General Atomics, San Diego, CA
 H. Yoshida, ITER Naka, Naka, Japan
 C.E.A. Library, Fontenay-aux-Roses, France
 Librarian, Culham Laboratory, England
 Thermonuclear Library, Japan Atomic Energy Research Institute, Japan
 University of Illinois, Fusion Studies Laboratory
 University of Illinois, Grainger Engineering Library Information Center